

# Recycled stellar ejecta as fuel for star formation and implications for the origin of the galaxy mass-metallicity relation

Marijke C. Segers,<sup>1\*</sup> Robert A. Crain,<sup>2,1</sup> Joop Schaye,<sup>1</sup> Richard G. Bower,<sup>3</sup>  
Michelle Furlong,<sup>3</sup> Matthieu Schaller<sup>3</sup> and Tom Theuns<sup>3</sup>

<sup>1</sup>*Leiden Observatory, Leiden University, PO Box 9513, NL-2300 RA Leiden, the Netherlands*

<sup>2</sup>*Astrophysics Research Institute, Liverpool John Moores University, 146 Brownlow Hill, Liverpool, L3 5RF, UK*

<sup>3</sup>*Institute for Computational Cosmology, Department of Physics, University of Durham, South Road, Durham DH1 3LE, UK*

Accepted XXX. Received YYY; in original form ZZZ

## ABSTRACT

We use cosmological, hydrodynamical simulations from the EAGLE and OWLS projects to assess the significance of recycled stellar ejecta as fuel for star formation. The fractional contributions of stellar mass loss to the cosmic star formation rate (SFR) and stellar mass densities increase with time, reaching 35% and 19%, respectively, at  $z = 0$ . The importance of recycling increases steeply with galaxy stellar mass for  $M_* < 10^{10.5} M_\odot$ , and decreases mildly at higher mass. This trend arises from the mass dependence of feedback associated with star formation and AGN, which preferentially suppresses star formation fuelled by recycling. Recycling is more important for satellites than centrals and its contribution decreases with galactocentric radius. The relative contribution of AGB stars increases with time and towards galaxy centers. This is a consequence of the more gradual release of AGB ejecta compared to that of massive stars, and the preferential removal of the latter by outflows and by lock up in stellar remnants. Recycling-fuelled star formation exhibits a tight, positive correlation with galaxy metallicity, with a secondary dependence on the relative abundance of alpha elements (which are predominantly synthesized in massive stars), that is insensitive to the subgrid models for feedback. Hence, our conclusions are directly relevant for the origin of the mass-metallicity relation and metallicity gradients. Applying the relation between recycling and metallicity to the observed mass-metallicity relation yields our best estimate of the mass-dependent contribution of recycling. For centrals with a mass similar to that of the Milky Way, we infer the contributions of recycled stellar ejecta to the SFR and stellar mass to be 35% and 20%, respectively.

**Key words:** galaxies: abundances – galaxies: formation – galaxies: haloes – galaxies: star formation

## 1 INTRODUCTION

The rate at which galaxies form stars is closely related to the amount of fuel that is available. Although we still lack a complete understanding of how galaxies obtain their gas, several potential sources of star formation fuel have been investigated in previous works, both observationally and using hydrodynamical simulations (e.g. Putman et al. 2009). Galaxies accrete gas from the intergalactic medium (IGM) along cold, dense, filamentary streams (e.g. Kereš et al. 2005; Dekel et al. 2009; Brooks et al. 2009; van de Voort & Schaye 2012), which can extend far inside the halo virial radius, and through quasi-spherical infall from a diffuse hot halo, which contains gas that has been shock-heated to the halo virial temperature (Rees & Ostriker 1977; Silk 1977). Cosmological, hydrodynamical simulations give predictions for the relative

importance of these two ‘modes’ of gas accretion, generally indicating a dominant role for the cold mode in the global build up of galaxies, with the hot mode becoming increasingly important towards lower redshifts and in more massive systems (e.g. Birnboim & Dekel 2003; Kereš et al. 2005, 2009; Crain et al. 2010; van de Voort et al. 2011; Nelson et al. 2013). Galaxies can also acquire new fuel for star formation by stripping the gas-rich envelopes of merging galaxies as soon as these become satellites in a group or cluster environment (e.g. Sancisi et al. 2008; van de Voort et al. 2011) or by re-accreting gas that has previously been ejected from the galaxy in an outflow and is raining back down in the form of a halo fountain (e.g. Oppenheimer & Davé 2008; Oppenheimer et al. 2010).

In addition to the various channels of accreting gas from the IGM, every galaxy has an internal channel for replenishing the reservoir of gas in the interstellar medium (ISM), namely the shedding of mass by the stellar populations themselves. Stars lose a

\* E-mail: segers@strw.leidenuniv.nl

fraction of their mass in stellar winds before and while they go through the asymptotic giant branch (AGB) phase. Furthermore, a substantial amount of stellar material is released as stars end their lives in supernova (SN) explosions. Eventually,  $\sim 50\%$  of the initial mass of a stellar population will be released. If this material is not ejected into the circumgalactic medium (CGM), where it can emerge as X-ray emitting gas in the hot circumgalactic corona (e.g. [Parriott & Bregman 2008](#); [Crain et al. 2013](#)), or entirely expelled from the galaxy into the IGM (e.g. [Ciotti et al. 1991](#)), but rather ends up in the cool ISM gas reservoir, then it can be ‘recycled’ to fuel subsequent generations of star formation (e.g. [Mathews 1990](#); [Martin et al. 2007](#)). Note that what we call ‘gas recycling’ here is different from the process considered in works on galactic outflow fountains, in which ‘recycling’ refers to the re-accretion of gas ejected from the ISM, regardless of whether it has ever been part of a star. In this work ‘recycled gas’ refers to the gas from evolved stars that is used to form new stars, regardless of whether it has been blown out of a galaxy.

Using observational constraints on the rates of gas infall and the history of star formation, [Leitner & Kravtsov \(2011\)](#) assessed the significance of recycled stellar evolution products in the gas budget of a number of nearby disk galaxies (including the Milky Way). They modeled the global mass loss history of each galaxy from an empirically motivated distribution of stellar population ages and a set of stellar yields and lifetimes, and showed that the gas from stellar mass loss can provide most of the fuel required to sustain the current rates of star formation. They suggested that this internal supply of gas is important for fuelling star formation at late epochs, when the cosmological accretion rate drops or is suppressed by preventative feedback (e.g. [Mo & Mao 2002](#)), hence falling short of the observed star formation rate (SFR) of the galaxies. Furthermore, [Voit & Donahue \(2011\)](#) argued that due to the high ambient pressures and the resulting short gas cooling times, central cluster galaxies are very efficient at recycling stellar ejecta into new stars. They showed that the stellar mass loss rates are generally comparable to, or even higher than, the observed rates of star formation and emphasized the importance of including this form of internal gas supply in any assessment of the gas budget of such systems. These conclusions are consistent with the observation by [Kennicutt et al. \(1994\)](#) that recycling of stellar ejecta can extend the lifetimes of gaseous discs by factors of  $1.5 - 4$ , enabling them to sustain their ongoing SFRs for periods comparable to the Hubble time (see also [Roberts 1963](#); [Sandage 1986](#)). These studies suggest that recycled stellar mass loss is an important part of the gas budget of star-forming galaxies, even hinting that it may be a necessary ingredient to reconcile the gas inflow and consumption rates of the Milky Way.

In this paper, we investigate the importance of gas recycling for fuelling star formation by explicitly calculating the contribution of stellar mass loss to the SFR and stellar mass of present-day galaxies. We use cosmological simulations from the Evolution and Assembly of GaLaxies and their Environments (EAGLE) project ([Schaye et al. 2015](#), hereafter S15; [Crain et al. 2015](#)) to explore the recycling of stellar ejecta, as a cosmic average as a function of redshift and within individual (central and satellite) galaxies at  $z = 0$ , where we give quantitative predictions for recycling-fuelled star formation as a function of galaxy stellar mass and establish a connection with observational diagnostics by relating these predictions to gas-phase and stellar metallicities. The EAGLE simulations explicitly follow the mass released by stellar populations in the form of stellar winds and SN explosions of Types Ia and II, enabling us to study the relative significance of these mass loss channels

for fuelling star formation. The subgrid parameters in the models for feedback associated with star formation and active galactic nuclei (AGN) have been calibrated to reproduce the  $z \simeq 0$  observed galaxy stellar mass function (GSMF) and the relation between stellar mass,  $M_*$ , and the mass of the central supermassive black hole (BH),  $M_{\text{BH}}$ , with the additional constraint that the sizes of disc galaxies must be reasonable. The EAGLE simulations not only successfully reproduce these key observational diagnostics with unprecedented accuracy, but are also in good agreement with a large and representative set of low- and high-redshift observables that were not considered during the calibration (S15, [Crain et al. 2015](#); [Furlong et al. 2015](#); [Lagos et al. 2015](#); [Rahmati et al. 2015](#); [Sawala et al. 2015](#); [Schaller et al. 2015](#)). This, in combination with the inclusion of a detailed chemodynamics model, makes EAGLE the ideal tool for making quantitative predictions on the importance of gas recycling for fuelling star formation.

We also briefly explore the sensitivity of our results to the physical processes in the subgrid model. To do so, we use a suite of cosmological simulations from the Overwhelmingly Large Simulations (OWLS) project ([Schaye et al. 2010](#)). As the OWLS project aimed to explore the role of the different physical processes modelled in the simulations, it covers a wide range of subgrid implementations and parameter values, including extreme variations of the feedback model and variations of the stellar initial mass function (IMF). We will show that the efficiency of the feedback associated with star formation and AGN plays an important role in regulating the fuelling of star formation with recycled stellar ejecta.

We note that, because of the tight correlation we find between the contribution of stellar mass loss to the SFR (stellar mass) and the ISM (stellar) metallicity, our characterization and explanation of the role of stellar mass loss as a function of galaxy mass and type has important and direct implications for the origin of the mass-metallicity relation.

This paper is organized as follows. In Section 2 we show the (metal) mass released by a simple stellar population as a function of its age. In Section 3 we present a brief overview of the simulation set-up and the subgrid modules implemented in EAGLE. In this section we also introduce the two quantities we use to assess the importance of gas recycling, namely the fractional contributions of stellar mass loss to the SFR and stellar mass. In Section 4 we present quantitative predictions from EAGLE for the evolution of the cosmic averages of these quantities and for their dependence on metallicity and galaxy stellar mass. We explore the sensitivity of these results using a set of OWLS simulations in Section 5. Finally, we summarize our findings in Section 6.

## 2 MASS RELEASED BY A SIMPLE STELLAR POPULATION

The amount of gas that galaxies can recycle to form new generations of stars, depends fundamentally on the fraction of stellar mass that is returned to the ISM. In cosmological, hydrodynamical simulations, a stellar population is represented by a ‘star particle’ and modelled as a population of stars of a single age and metallicity, referred to as a simple stellar population (SSP). Since the recycling of SSP mass loss is key to this work, we start by investigating how much mass of gas and metals is released as a function of SSP age as specified by the stellar evolution model of [Wiersma et al. \(2009b\)](#), which is adopted by the simulations used in this work. We summarize the main ingredients of the model and present its outcome

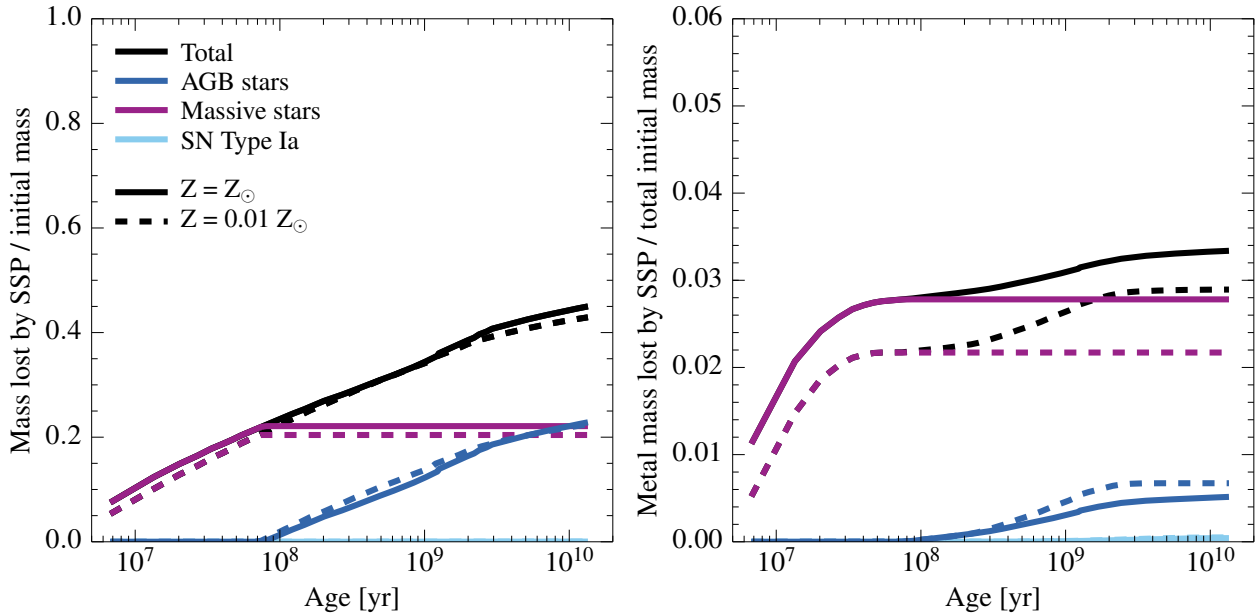


**Figure 1.** The cumulative fraction of the initial mass (total: left panel; in the form of metals, i.e. elements heavier than helium: right panel) that is released by an SSP as a function of its age, adopting a [Chabrier \(2003\)](#) IMF in the range  $0.1 - 100 M_{\odot}$ . The curves show the contributions from AGB stars (blue), massive stars (purple) and SN Type Ia (cyan), as well as the total (metal) mass ejected by the SSP (black), for two stellar metallicities: solar (solid) and 1 percent of solar (dashed). Initially, all the ejected (metal) mass comes from massive stars, but for SSP ages  $\gtrsim 10^8$  yr the contribution from AGB stars becomes increasingly significant. The contribution from SN Type Ia to the (metal) mass loss remains insignificant at all times. Changing the metallicity does not have a strong effect on the total mass loss, but increases the total ejected metal mass as well as the relative contribution from massive stars. Comparing, for each channel, the total to the metal mass loss shows that the ejecta from massive stars are more metal-rich than those from AGB stars.

for two stellar IMFs: a [Chabrier \(2003\)](#) IMF (this section) and a [Salpeter \(1955\)](#) IMF (Appendix A).

The model considers the mass released by both intermediate- and high-mass stars. Massive stars enrich their environments through stellar winds and by means of supernova explosions (SN Type II) at the end of their lives. Intermediate-mass stars undergo phases of mass loss during the AGB phase. Furthermore, intermediate-mass stars that accrete mass from a binary companion can end their lives in SN Type Ia explosions.

The choice of IMF, which determines the distribution of mass among the stars in the population, is the first important ingredient of the stellar evolution model. A top-heavy IMF yields a population with relatively many intermediate-mass and massive stars per unit stellar mass formed. Hence, for this type of IMF, the fraction of mass lost by the stellar population is high. Conversely, for a bottom-heavy IMF with many low-mass stars (e.g. Salpeter), relatively few stars contribute to the mass loss and the fraction of mass returned to the ISM is low. [Leitner & Kravtsov \(2011\)](#) show that the difference in mass loss between alternative, reasonable choices of the IMF can be significant (see their fig. 1). We similarly conclude in Appendix A that the total mass loss is a factor of  $\sim 1.5$  higher for a Chabrier IMF than for a Salpeter IMF. Furthermore, as high-mass stars are the main synthesizers of heavy elements (in terms of mass fraction), a population with a top-heavy IMF releases a higher mass of metals into the ISM, which boosts the gas cooling rate and may reduce the efficiency of galactic winds. This may in turn compensate for the extra energy from SN Type II that is injected into the gas. In this section we consider the Chabrier IMF, which is adopted by both the EAGLE and OWLS simulations (except for those OWLS models in which the IMF is explicitly varied).

The results for the more bottom-heavy Salpeter IMF, used by one of the OWLS model variations examined in Section 5, are presented in Appendix A. For both IMFs we assume a mass range of  $0.1 - 100 M_{\odot}$ .

As detailed in [Wiersma et al. \(2009b\)](#), the timed release of mass by an SSP with a given initial mass and metallicity is calculated using the metallicity-dependent stellar lifetime tables of [Portinari et al. \(1998\)](#), in combination with the complete set of nucleosynthetic yields of [Marigo \(2001\)](#) and [Portinari et al. \(1998\)](#), all of which are based on the same Padova evolutionary tracks, and the SN Type Ia yields of the W7 model of [Thielemann et al. \(2003\)](#). [Marigo \(2001\)](#) specify the mass lost by intermediate-mass stars in the mass range  $0.8 - 6 M_{\odot}$  as they go through the AGB phase. The mass loss and nucleosynthesis occurring in massive stars in the mass range  $6 - 100 M_{\odot}$  is given by [Portinari et al. \(1998\)](#), who add pre-SN stellar mass loss to the SN Type II yields from [Woosley & Weaver \(1995\)](#). [Thielemann et al. \(2003\)](#) specify the yields from intermediate-mass stars in the mass range  $3 - 8 M_{\odot}$  as they end their lives in a SN Type Ia explosion. Because these events are the result of binary evolution, one cannot assign a single lifetime to their progenitors. Therefore, the distribution of progenitor lifetimes is modelled using an empirically motivated time-delay function that is calibrated to the observed cosmic SN Type Ia rate (see fig. 3 of S15).

The stellar lifetimes and the nucleosynthetic yields both depend on the initial composition of the stellar population. We therefore consider the mass loss from an SSP adopting two different metallicities: solar and 1 percent of solar, using a solar value of  $Z_{\odot} = 0.0127$ . The left panel of Fig. 1 shows the mass released by an SSP as a function of its age assuming a [Chabrier \(2003\)](#)

IMF. The curves show the total integrated mass ejected by the SSP (black) and the integrated mass sourced by AGB stars (blue), massive stars (i.e. stellar winds plus SN Type II; purple) and SN Type Ia (cyan). The ejected mass is expressed as a fraction of the total initial mass of the SSP.

As the SSP ages, it ejects an increasing fraction of its mass. It has lost over 40% when it is older than  $10^{10}$  yr. Initially, only massive stars contribute to the mass loss, but for ages  $\gtrsim 10^8$  yr the contribution from AGB stars becomes increasingly significant. For SN Type Ia, on the other hand, the contribution to the overall mass loss remains insignificant for all SSP ages.

The adoption of a different metallicity (solar: solid; 0.01 times solar: dashed) for the SSP does not alter the time-dependent mass loss strongly. A higher metallicity tends to slightly increase the mass lost by massive stars and to slightly decrease the mass lost by AGB stars (for ages  $\lesssim 10^9$  yr). This changes their relative contributions to the mass loss, but only by a few percent. We conclude that the initial metallicity of a stellar population does not have a strong effect on the mass of gas that is recycled back into ISM, at least for the metallicities considered here.

Since radiative cooling rates, and thereby the efficiency with which galaxies form stars and drive galactic outflows, are sensitive to the galactic metal abundance, we show in the right panel of Fig. 1 the metal mass released by the SSP, expressed as a cumulative fraction of the total initial mass. Note that the scale on the vertical axis is different from that of the left panel. As was the case for the total mass loss, the release of metal mass is initially due solely to massive stars. For ages  $\gtrsim 10^8$  yr, AGB stars also begin to contribute. However, even for evolved populations, the metal mass released by AGB stars remains substantially lower than the contribution from massive stars, because the ejecta from AGB stars are less metal-rich. The metal mass loss due to SN Type Ia is insignificant for all SSP ages.

Note that we have only considered the relative contributions from massive and intermediate-mass stars to the total ejected metal mass, which may be different from their contributions to the ejected mass of individual elements. For example, SN Type Ia are an important source of iron, their fractional contribution to the released Fe abundance increasing with time up to  $\sim 30\% - 40\%$  (Wiersma et al. 2009b). The difference in timescales of Fe enrichment by SN Type Ia and  $\alpha$ -element enrichment by massive stars, which detonate almost instantaneously, is the reason that  $[\alpha/\text{Fe}]$  is often used as a galactic chronometer. However, compared to the total metal mass, the mass released in the form of iron is negligible. Hence, despite their role in shaping the relative elemental abundances in galaxies, SN Type Ia do not contribute significantly to the total metal mass released by stellar populations.

Finally, compared to the total mass lost by the SSP, the release of metals is more strongly affected by the metallicity of the SSP. Adopting a higher metallicity increases the total ejected metal mass, as well as the relative contribution from massive stars.

### 3 SIMULATIONS

Having calculated the mass released by an SSP, we turn to simulations to investigate how much of this mass is actually used to fuel star formation in galaxies. Due to the variety of processes, such as cosmological infall, gas stripping of satellite galaxies, and feedback associated with star formation and AGN, that can have an effect on the star formation histories of individual galaxies, it is not straightforward to calculate this analytically. In this work, we use

a cosmological simulation from the EAGLE project to investigate the contribution of recycled stellar mass loss to the SFR and stellar mass of present-day central and satellite galaxies. In this section we first briefly describe the implementation of the EAGLE simulation and give an overview of the different physical processes that were included in the subgrid physics. For more details we refer the reader to S15.

While most of the results presented in this work are derived from the EAGLE simulation, we also perform a model comparison using a suite of cosmological simulations from the OWLS project (Schaye et al. 2010) to explore the effect of the different feedback processes and the choice of the IMF on gas recycling. The results of this comparison are presented in Section 5, where we also briefly describe the OWLS simulations used.

The EAGLE simulations were run with a modified version of the smoothed particle hydrodynamics (SPH) code GADGET3 (last described in Springel 2005) using a pressure-entropy formulation of SPH (Hopkins 2013). While EAGLE is actually a suite of simulations, we will in this work primarily use the largest EAGLE simulation, which we will refer to as *Ref-L100N1504* (as in S15) or as the ‘fiducial’ model. This simulation was run in a periodic volume of size  $L = 100$  comoving Mpc (cMpc), containing  $N = 1504^3$  dark matter particles and an equal number of baryonic particles. However, when we test for numerical convergence (Appendix B), we use a set of three simulations that were run in volumes of size  $L = 25$  cMpc, either with the same resolution as the fiducial model ( $N = 376^3$ ) or with 8 times better mass resolution ( $N = 752^3$ ). This includes a high-resolution simulation, which we will refer to as *Recal-L025N0752* (as in S15), whose subgrid feedback parameters were recalibrated to improve the fit to the observed present-day GSMF.

The EAGLE simulations were run to redshift  $z = 0$  and assume a  $\Lambda$ CDM cosmology with parameters  $[\Omega_m, \Omega_b, \Omega_\Lambda, \sigma_8, n_s, h] = [0.307, 0.04825, 0.693, 0.8288, 0.9611, 0.6777]$  (Planck Collaboration et al. 2014). The gravitational softening length was kept fixed in comoving units at  $1/25$  of the mean dark matter particle separation before  $z = 2.8$  and was switched to a fixed proper scale thereafter.

In the fiducial model, the particle masses for baryons and dark matter are initially  $m_b = 1.8 \times 10^6 M_\odot$  and  $m_{\text{dm}} = 9.7 \times 10^6 M_\odot$ , respectively. However, during the course of the simulation the masses of the baryonic particles change due to the process of mass transfer from star particles to gas particles. This transfer of mass plays a central role in our work, as it corresponds to the recycling of mass from a stellar population back into the gas reservoir.

#### 3.1 Subgrid physics

The subgrid physics used in EAGLE is largely based on the set of subgrid recipes developed for OWLS. These include prescriptions for radiative cooling and heating, star formation, stellar evolution, feedback associated with star formation, growth of BHs and feedback from AGN. While OWLS aimed to employ a wide range of subgrid implementations to investigate the sensitivity of galactic properties to the different physical processes, the subgrid routines in EAGLE have been *calibrated* to reproduce observations of the present-day GSMF, the  $M_* - M_{\text{BH}}$  relation and to yield reasonable galaxy sizes.

- Radiative cooling and heating are implemented following Wiersma et al. (2009a). The net cooling rates of 11 individual el-

elements (H, He, C, N, O, Ne, Mg, Si, S, Ca and Fe) are computed with the photoionization package CLOUDY (described in [Ferland et al. 1998](#)). Variations in the relative abundances of these elements and photoionization by UV and X-ray background radiation (using the model by [Haardt & Madau 2001](#)) are taken into account. The gas is assumed to be optically thin and in ionization equilibrium.

- Star formation is modelled according to the prescription of [Schaye & Dalla Vecchia \(2008\)](#). Gas particles that are above a metallicity-dependent density threshold,  $n_{\text{H}}^*(Z)$  (given by [Schaye 2004](#)), become eligible for star formation. They are assigned a pressure-dependent SFR and are stochastically converted into star particles, such that the relation between star formation rate surface density and gas surface density matches the observed relation by [Kennicutt \(1998\)](#). Because the cold phase of the ISM is unresolved, a global temperature floor,  $T_{\text{eos}}(\rho)$ , is imposed, which corresponds to a polytropic equation of state (EoS),  $P_{\text{eos}} \propto \rho^{4/3}$ , where  $P$  is the pressure and  $\rho$  is the mass density of the gas. This EoS is normalised to  $T_{\text{eos}} = 8000$  K at  $n_{\text{H}} = 0.1 \text{ cm}^{-3}$ .

- Stellar evolution and chemical feedback are implemented using the prescription of [Wiersma et al. \(2009b\)](#). The abundances of the 11 elements that dominate the radiative cooling rate are followed. A star particle, representing an SSP, inherits its mass and metallicity from its progenitor gas particle, but over the course of time it loses mass through the release of mass by both massive and intermediate-mass stars (as discussed in Section 2). Every gravitational time step (every 10th time step for star particles older than 100 Myr), the ejecta are distributed over the neighbouring gas particles according to the SPH interpolation scheme<sup>1</sup>. Hence, a fraction of the mass of these enriched gas particles comes from the evolving stellar population. When this gas becomes eligible for star formation, the stellar ejecta are recycled as they contribute to a new generation of stars.

- Energy feedback from star formation (i.e. the prompt energy feedback from SN Type II and the winds from their massive progenitor stars) is implemented thermally as described in [Dalla Vecchia & Schaye \(2012\)](#). Gas particles are stochastically heated by their neighbouring star particles by a temperature  $\Delta T = 10^{7.5}$  K. This happens once per star particle, 30 Myr after its formation. Imposing a fixed, stochastic temperature jump, rather than heating all gas particles within the SPH kernel continuously, results in longer gas cooling times and allows the thermal energy to be efficiently converted into kinetic energy. The feedback energy available from SNe is based on assuming that all stars in the mass range 6 – 100  $M_{\odot}$  release  $10^{51}$  erg of energy into the ISM, consistent with the adopted [Chabrier \(2003\)](#) IMF. A fraction  $f_{\text{th}}$  of the total available energy is injected into the gas, where  $f_{\text{th}}$  depends on the local gas metallicity and density in such a way that on average  $f_{\text{th}} \approx 1$  (see S15 and [Crain et al. 2015](#) for details).

- Finally, the subgrid physics includes prescriptions for the formation and growth of BHs, and the feedback from AGN. Following [Springel et al. \(2005\)](#), BH particles with seed mass  $m_{\text{seed}} = 10^5 h^{-1} M_{\odot}$  are inserted into haloes more massive than  $m_{\text{halo,min}} = 10^{10} h^{-1} M_{\odot}$ . The BH seeds can grow either through the accretion of ambient gas, at a rate that depends on the

angular momentum of the gas limited by the Eddington rate (S15; [Rosas-Guevara et al. 2013](#)), or through mergers with other BHs. The amount of energy available for AGN feedback is related to the BH accretion rate  $\dot{m}_{\text{acc}}$ , the radiative efficiency  $\epsilon_{\text{r}}$  of the BH and the fraction  $\epsilon_{\text{f}}$  of the radiated energy that couples to the ISM:  $\dot{E}_{\text{feed}} = \epsilon_{\text{f}} \epsilon_{\text{r}} \dot{m}_{\text{acc}} c^2$ , where  $c$  is the speed of light. Using the model developed by [Booth & Schaye \(2009\)](#) and S15, AGN feedback is implemented thermally by stochastically heating neighbouring gas particles by a temperature  $\Delta T (= 10^{8.5}$  K in the fiducial EAGLE model). The BH becomes eligible to heat its surroundings once it has stored sufficient energy to heat at least one gas particle by the required temperature jump.

## 3.2 Numerical convergence

For the high-resolution *Recal-L025N0752* simulation the stellar and AGN feedback were recalibrated to the same observational diagnostics as the fiducial *Ref-L100N1504* model (see S15 for a discussion on the need for recalibration upon changing the resolution). In short, the recalibration corresponds to a change in the density dependence of  $f_{\text{th}}$ , in order to compensate for the increase in cooling losses that arise in the locally higher gas densities resolved by the simulation ([Crain et al. 2015](#)). This yields a set of subgrid parameter values, listed in table 3 of S15, that are slightly different from the ones used in the fiducial model. The *Recal-L025N0752* simulation enables us to perform a ‘weak’ numerical convergence test, i.e. a comparison between different resolution simulations with the subgrid model calibrated at the respective resolutions. We briefly show such a comparison when we present results as a function of halo and stellar mass in Section 4.3, while a more detailed convergence test can be found in Appendix B1. In the rest of the results section (Section 4) we only use the fiducial simulation, which, due to its 64 times larger volume than *Recal-L025N0752*, provides a better statistical sample of the massive galaxy population and models a more representative volume of the Universe.

## 3.3 Identifying haloes and galaxies

Haloes are identified using a Friends-of-Friends (FoF) algorithm ([Davis et al. 1985](#)), linking dark matter particles that are separated by less than 0.2 times the mean interparticle separation. Gas and star particles are assigned to the same halo group as their nearest dark matter particle. The SUBFIND algorithm ([Springel et al. 2001](#); [Dolag et al. 2009](#)) then searches for gravitationally bound substructures within the FoF haloes, which we label ‘galaxies’ if they contain stars. The galaxy position is defined to be the location of the particle with the minimum gravitational potential within the subhalo. The galaxy at the absolute minimum potential in the FoF halo (which is almost always the most massive galaxy) is classified as the ‘central’ galaxy, whereas the remaining subhaloes are classified as ‘satellite’ galaxies.

The mass of the main halo,  $M_{200}$ , is defined as the mass internal to a spherical shell centred on the minimum gravitational potential, within which the mean density equals 200 times the critical density of the Universe. The subhalo mass,  $M_{\text{sub}}$ , corresponds to all the mass bound to the substructure identified by SUBFIND. The stellar mass,  $M_*$ , refers to the total mass in stars that is bound to this substructure and that resides within a 3D spherical aperture of radius 30 pkpc. Other galaxy properties, such as the SFR and the stellar half-mass radius, are also computed considering only particles within this aperture, mimicking observational measurements of

<sup>1</sup> As discussed in S15 and different from [Wiersma et al. \(2009b\)](#), EAGLE uses weights that are independent of the current gas particle mass for the distribution of stellar mass loss. The reason for this is to avoid a runaway process, causing a small fraction of the particles to end up with very large masses compared to their neighbours, as particles that have grown massive due to enrichment, are also likely to become increasingly enriched in future time steps, if they carry more weight in the interpolation.

these quantities (as shown in fig 6. of S15, the present-day GSMF using a 30 pkpc 3D aperture is nearly identical to the one using the 2D Petrosian aperture applied by SDSS). The aperture has negligible effects on stellar masses for  $M_* < 10^{11} M_\odot$  and galactic SFRs, as the vast majority of the star formation takes place within the central 30 pkpc. For the more massive galaxies, on the other hand, the stellar masses are somewhat reduced, as the aperture cuts out the diffuse stellar mass at large radii that would contribute to the intracluster light.

### 3.4 Measuring the star formation rate and stellar mass contributed by recycling

The two main quantities that we use to indicate the importance of gas recycling for fuelling star formation in galaxies are  $SFR_{\text{rec}}$  and  $M_{*,\text{rec}}$ . These correspond to the SFR and the stellar mass, respectively, that is contributed by mass released by evolved stellar populations. These two quantities are related, as one can obtain the stellar mass by integrating the SFR over time (while taking into account stellar mass loss). It is, however, still helpful to consider both. While  $SFR_{\text{rec}}$  indicates the instantaneous impact of gas recycling,  $M_{*,\text{rec}}$  provides complementary information by indicating the importance of recycling over the past history of star formation. Furthermore, while  $SFR_{\text{rec}}$  can in principle account for all SFR at the respective time, the stellar mass of a galaxy cannot be exclusively contributed by gas recycling, as some fraction of the unprocessed gas is unavoidably locked up in stellar remnants. We measure these quantities from the simulations as follows.

At the start of each simulation, all gas particles have the same mass  $m_b$ . Over the course of time, some gas particles are converted into star particles and start shedding an increasing fraction of their mass as the SSPs evolve. Neighbouring gas particles then become enriched with stellar ejecta (in the form of hydrogen, helium and heavy elements), and their masses grow over time. At time  $t$ , the total mass fraction of gas from released stellar material in a particle of current mass  $m_g^i(t)$  is given by

$$f_{g,\text{rec}}^i(t) = \frac{m_g^i(t) - m_b}{m_g^i(t)}. \quad (1)$$

Since a gas particle is the smallest quantum of mass we are able to consider, its recycled fraction is by construction assumed to be perfectly mixed. Therefore, if the gas particle is considered star-forming,  $f_{g,\text{rec}}^i(t)$  also indicates the fraction of its current SFR that is contributed by stellar mass loss. Then, summing up the contributions from all  $N_g^{\text{gal}}$  gas particles in a galaxy (within the 30 pkpc 3D aperture) yields the aforementioned quantity for this galaxy:

$$SFR_{\text{rec}}^{\text{gal}}(t) = \sum_{i=1}^{N_g^{\text{gal}}} \frac{m_g^i(t) - m_b}{m_g^i(t)} SFR^i(t), \quad (2)$$

where  $m_g^i(t)$  is the mass and  $SFR^i(t)$  is the SFR of gas particle  $i$  at time  $t$ . Similarly, summing up the contributions from all  $N_g^{\text{cos}}$  gas particles in the simulation volume yields the cosmic average of this quantity:

$$SFR_{\text{rec}}^{\text{cos}}(t) = \sum_{i=1}^{N_g^{\text{cos}}} \frac{m_g^i(t) - m_b}{m_g^i(t)} SFR^i(t). \quad (3)$$

Since a star particle inherits its mass and elemental abundances from its progenitor gas particle, the fraction of its mass con-

tributed by recycling is:

$$f_{*,\text{rec}}^j(t) = \frac{m_{*,\text{init}}^j - m_b}{m_{*,\text{init}}^j}, \quad (4)$$

where  $m_{*,\text{init}}^j = m_g^j(t_{\text{birth}})$  is the mass of star particle  $j$  at the time of its birth,  $t_{\text{birth}}$ . Note that equation (4) is valid for all  $t \geq t_{\text{birth}}$ , even though the star particle itself loses mass. This is again a consequence of the assumption of perfect mixing on the particle scale. Summing up the contributions from all  $N_*^{\text{gal}}$  star particles in a galaxy that are within the 3D aperture,

$$M_{*,\text{rec}}^{\text{gal}}(t) = \sum_{j=1}^{N_*^{\text{gal}}} \frac{m_{*,\text{init}}^j - m_b}{m_{*,\text{init}}^j} m_*^j(t), \quad (5)$$

and all  $N_*^{\text{cos}}$  star particles in the simulation volume,

$$M_{*,\text{rec}}^{\text{cos}}(t) = \sum_{j=1}^{N_*^{\text{cos}}} \frac{m_{*,\text{init}}^j - m_b}{m_{*,\text{init}}^j} m_*^j(t), \quad (6)$$

give the galaxy stellar mass and cosmic stellar mass, respectively, contributed by recycled gas.

In this work we mainly focus on the *relative* contribution of gas recycled from stellar mass loss to the total (cosmic or galactic) SFR and stellar mass. Normalizing  $SFR_{\text{rec}}$  and  $M_{*,\text{rec}}$  by the respective total quantities, yields  $SFR_{\text{rec}}/SFR$  and  $M_{*,\text{rec}}/M_*$ , specifying the *fractions* of the SFR and the stellar mass that are due to stellar mass loss.

In addition to the total amount of recycling, we will also consider the relative contributions from the different sources of stellar mass loss that were included in the subgrid model (Section 2). As the transfer of mass from AGB stars, SN Type Ia and massive stars between star and gas particles is explicitly followed in the EAGLE simulation, we can calculate  $SFR_{\text{rec}}/SFR$  and  $M_{*,\text{rec}}/M_*$  solely due to gas from AGB stars by simply replacing  $m_g^i(t) - m_b$  in equations (2) and (3) by  $m_{\text{AGB}}^i$  and replacing  $m_{*,\text{init}}^j - m_b$  in equations (5) and (6) by  $m_{\text{AGB}}^j$ , where  $m_{\text{AGB}}$  is the mass from AGB stars in the respective gas or star particle. The  $SFR_{\text{rec}}/SFR$  and  $M_{*,\text{rec}}/M_*$  due to gas from SN Type Ia and massive stars are calculated analogously.

## 4 RECYCLED STELLAR MASS LOSS IN EAGLE

In this section we use the fiducial EAGLE simulation, *Ref-L100N1504*, to make quantitative predictions for the importance of gas recycling for fuelling ongoing star formation in present-day galaxies over a wide range of galaxy masses.

If  $SFR_{\text{rec}}/SFR$  and  $M_{*,\text{rec}}/M_*$  (calculated using equations 2 and 5) are low, then this could mean that the galaxy has a high infall rate of unprocessed, ‘non-recycled’ gas, resulting in a high total  $SFR$  compared to  $SFR_{\text{rec}}$ . Note that this does not imply that most of the SFR and stellar mass is in the form of Pop III (i.e. metal-free) stars, because the stellar evolution products are mixed with the unprocessed material (in the simulations on the scale of a gas particle). Low values of  $SFR_{\text{rec}}/SFR$  and  $M_{*,\text{rec}}/M_*$  could also mean that the gas released by stellar populations is efficiently ejected from the galaxy due to stellar or AGN feedback. As we will show explicitly from our model comparison in Section 5, the feedback associated with star formation and AGN reduces the contribution from recycled gas to the SFR and stellar mass, if these feedback processes drive galactic winds. The reason is that these

winds are launched from the dense star-forming regions with relatively high abundances of gas from stellar mass loss, thereby preferentially reducing  $SFR_{\text{rec}}$  with respect to the total  $SFR$ . On the other hand, high values of  $SFR_{\text{rec}}/SFR$  can arise if the infall of fresh gas onto the galaxy is reduced (e.g. once a hot hydrostatic halo has formed), leaving stellar mass loss as the main source of star formation fuel, or if the feedback from star formation and AGN is ineffective at driving galactic outflows, allowing the build up of large amounts of released stellar material.

Before exploring gas recycling in individual galaxies at  $z = 0$ , we first investigate how recycling-fuelled star formation evolves over cosmic history. To this end, we study how  $SFR_{\text{rec}}/SFR$  and  $M_{*,\text{rec}}/M_*$  in the cosmological volume of the EAGLE simulation box (i.e. calculated from *Ref-L100N1504* using equations 3 and 6) evolve between  $z = 10$  and 0.

#### 4.1 Evolution of the cosmic average

The left panel of Fig. 2 shows the total cosmic SFR density (black), the cosmic SFR density fuelled by stellar mass loss (red, solid: ‘recycled’) and the cosmic SFR density fuelled by unprocessed gas (blue: ‘non-recycled’) as a function of redshift. The red curve has been split into the contributions from the three mass loss channels that are tracked by the simulation: AGB stars (dashed), massive stars (dotted) and SN Type Ia (dot-dashed). To get a better idea of the evolution of the *fractional* contribution from recycled gas to the cosmic star formation history, we show the evolution of the cosmic average  $SFR_{\text{rec}}/SFR$ , as well as the fractional contribution per channel, in Fig. 3 (red).

At  $z > 2$  there is little difference between the SFR density due to ‘non-recycled’ gas and the total SFR density. At these high redshifts most of the fuel for star formation is due to unprocessed gas, since there has simply not been much time for stellar populations to evolve and to distribute a significant amount of gas that can be recycled. From the ‘recycled’ curve we see that the SFR density fuelled by recycled stellar mass loss rises rapidly at high redshift, peaks at  $z \approx 1.3$ , and then declines steadily towards  $z = 0$ . This trend is similar to the evolution of the total SFR density, although with a delay of  $\sim 1.5$  Gyr (the total SFR density peaks at  $z \approx 2$ ). Furthermore, the slope of the ‘recycled’ curve is steeper at high redshift and shallower at low redshift compared to that of the total SFR density, indicating that gas recycling becomes increasingly important for fuelling star formation. This is consistent with the rapid rise of the total  $SFR_{\text{rec}}/SFR$  with decreasing redshift in Fig. 3. Our fiducial EAGLE model indicates that 35% of the present-day cosmic SFR density is fuelled by recycled stellar mass loss.

Comparing the different sources of stellar mass loss, we see that massive stars initially account for the majority of the SFR density from recycled gas. These stars have short lifetimes and are therefore the first to contribute to the mass loss from a stellar population (see Fig. 1). Towards lower redshift the mass lost by AGB stars becomes increasingly important and becomes the dominant contributor to the SFR density from recycled gas for  $z \lesssim 0.4$ . As expected from Fig. 1, recycled SN Type Ia ejecta do not contribute significantly to the cosmic SFR density at any redshift.

The right panel of Fig. 2 shows the build up of the cosmic stellar mass density, the total as well as the contributions from recycled and unprocessed gas. The evolution of the cosmic average,  $M_{*,\text{rec}}/M_*$ , is shown in Fig. 3 (blue). The stellar mass density is related to the SFR density, as one can calculate the former by integrating the latter over time (while taking into account stellar mass loss). Hence, similar to the SFR density, the stellar mass density

is initially ( $z \gtrsim 2$ ) dominated by star formation from unprocessed gas, while the contribution from recycling becomes increasingly important towards  $z = 0$ . EAGLE indicates that, at the present day, 19% of the cosmic stellar mass density has been formed from recycled stellar mass loss.

If we consider the relative significance of gas from intermediate- and high-mass stars, we again see that at high redshift massive stars account for the majority of the stellar mass formed from recycled gas, while the contribution from AGB stars becomes increasingly important with time. In this case, however, the gas recycled from massive stars remains at all redshifts the main contributor to the cosmic stellar mass density that is built up through recycling.

#### 4.2 Relation with metallicity at $z = 0$

Having studied the evolution of the cosmic average  $SFR_{\text{rec}}/SFR$  and  $M_{*,\text{rec}}/M_*$ , we will now take a closer look at the  $z = 0$  values for individual galaxies in the *Ref-L100N1504* simulation. In the next section we will give predictions for the fuelling of star formation by recycled stellar ejecta in present-day central and satellite galaxies as a function of their halo and stellar mass. To be able to relate these predictions to observational diagnostics, we first explore the relation between recycling-fuelled star formation and present-day metallicity. We will show that the fact that metals are synthesized in stars and are distributed over the ISM as the evolving stellar populations lose mass, makes them an excellent observational proxy for the contribution of stellar ejecta to the SFR and stellar mass.

We note that because  $SFR_{\text{rec}}/SFR$  and  $M_{*,\text{rec}}/M_*$  are not defined for subhaloes with  $\sum_i SFR^i = 0$  and  $\sum_j m_*^j = 0$ , respectively, we only consider (here and in what follows) subhaloes with a non-zero<sup>2</sup> SFR when assessing the former and only subhaloes with a non-zero stellar mass when assessing the latter. Our fiducial simulation contains 44 248 subhaloes with a non-zero SFR and 325 561 subhaloes with a non-zero stellar mass. In this section, however, where we study the  $SFR_{\text{rec}}/SFR$  and  $M_{*,\text{rec}}/M_*$  as a function of metallicity, we additionally require the subhaloes to have a galaxy stellar mass corresponding to at least 100 gas particles in order to obtain adequate sampling of galaxy metallicities (in the next section we do plot the results at lower mass scales, but we show them as dotted lines). This yields samples of 14 028 and 16 681 subhaloes, respectively.

Fig. 4 shows the fraction of the SFR (left panel) and stellar mass (right panel) fuelled by recycling as a function of, respectively, the mass-weighted absolute metallicity  $Z_{\text{gas}}$  of ISM gas (i.e. star-forming gas) and the mass-weighted absolute metallicity  $Z_*$  of stars, both for present-day central galaxies<sup>3</sup>. We find strong correlations between these quantities, with more metal-rich galaxies having a larger fraction of their SFR and stellar mass contributed by recycling. The figure reveals tight power-law relations between  $SFR_{\text{rec}}/SFR$  and  $Z_{\text{gas}}$ , characterized by a Pearson correlation coefficient of 0.95, and between  $M_{*,\text{rec}}/M_*$  and  $Z_*$ , with a correlation coefficient of 0.99. For the former we find a  $1\sigma$  scatter of  $\sim 0.1 - 0.2$  dex for  $Z_{\text{gas}} < 10^{-1.9}$  and  $\lesssim 0.05$  dex for

<sup>2</sup> ‘Non-zero’ means containing at least one star-forming gas particle, which corresponds to a specific SFR ( $= SFR/M_*$ ) of  $> 10^{-12} \text{ yr}^{-1}$  at  $M_* \sim 10^9 M_\odot$  and  $> 10^{-14} \text{ yr}^{-1}$  at  $M_* \sim 10^{11} M_\odot$ .

<sup>3</sup> Although we do not explicitly show it, the results for central galaxies presented in this section are consistent with the results for satellite galaxies.

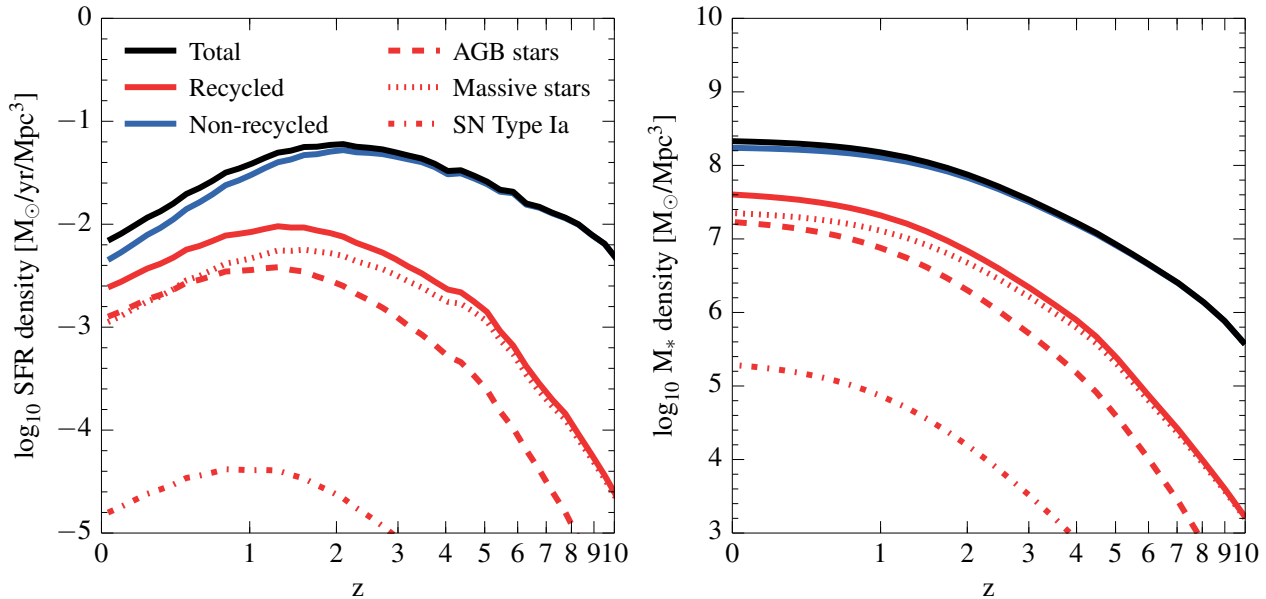


**Figure 2.** The evolution of the cosmic SFR density (left) and the cosmic stellar mass density (right) fuelled by recycled stellar mass loss (red), as well as the SFR and stellar mass densities fuelled by all gas (black) and gas that has not been recycled (blue). The ‘recycled’ SFR and stellar mass densities are split according to the contributions from AGB stars (dashed), massive stars (dotted) and SN Type Ia (dot-dashed). Recycling of stellar mass loss becomes increasingly important for fuelling star formation towards the present day. The gas from massive stars accounts for the majority of the cosmic SFR and stellar mass density from recycled gas at high redshift, but the contribution from AGB stars increases with time (accounting for the majority of the ‘recycled’ SFR density for  $z \lesssim 0.4$ ).

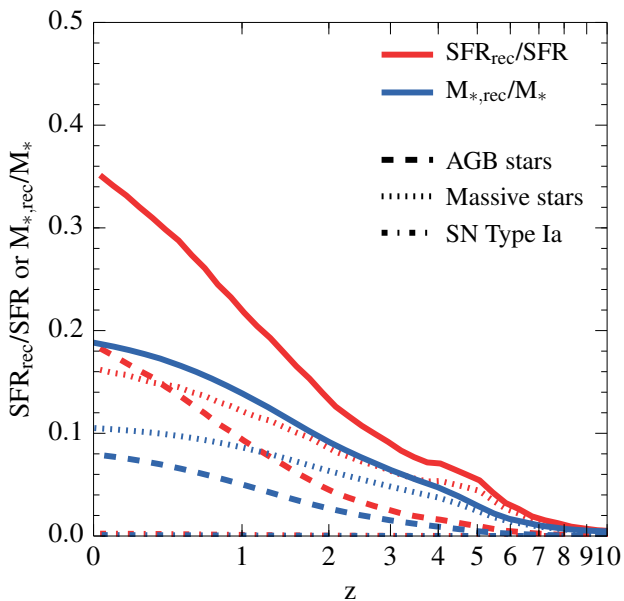


**Figure 3.** The evolution of the fractional contribution of recycled stellar mass loss to the cosmic SFR density (red) and cosmic stellar mass density (blue), where we show the total (solid) as well as the contributions from AGB stars (dashed), massive stars (dotted) and SN Type Ia (dot-dashed). With decreasing redshift, an increasing fraction of the cosmic SFR and stellar mass density is fuelled by recycled gas, which we find to be 35% and 19%, respectively, at  $z = 0$ .

$Z_{\text{gas}} > 10^{-1.9}$ , while for the latter we find an even smaller  $1\sigma$  scatter of  $\sim 0.01 - 0.03$  dex. Furthermore, as we show in Appendix B2, both relations are converged with respect to the numerical resolution.

The tight relation between the contribution of recycled gas to star formation and metallicity is not surprising considering that heavy elements were produced in stars and that their abundance must therefore correlate with the importance of stellar ejecta as star formation fuel. The contribution of recycling to the stellar mass is equal to the ratio of the mean stellar metallicity ( $\langle Z_* \rangle$ ) and the mean metallicity of the ejecta ( $\langle Z_{\text{ej}} \rangle$ ) that were incorporated into the stars,  $M_{*,\text{rec}}/M_* = \langle Z_* \rangle / \langle Z_{\text{ej}} \rangle$ . The same holds for the contribution of stellar mass loss to the SFR,  $SFR_{\text{rec}}/SFR = \langle Z_{\text{gas}} \rangle / \langle Z_{\text{ej}} \rangle$ . The metallicity of the ejecta depends on the age and metallicity of the SSP, as well as on the IMF. From Fig. 1 we can see that for our (Chabrier) IMF,  $\langle Z_{\text{ej}} \rangle \approx 0.033/0.45 \approx 0.073$  for a 10 Gyr old SSP with solar metallicity. Hence,  $\log_{10} M_{*,\text{rec}}/M_* \approx \log_{10} Z_* + 1.1$ , where the slope and normalization are close to the best-fit values that we determine below. Note that using ages of 100 Myr and 10 Myr instead of 10 Gyr gives normalizations of 0.91 and 0.77, respectively. Using an age of 10 Gyr but a stellar metallicity of  $0.01 Z_{\odot}$  instead of  $Z_{\odot}$  yields a normalization of 1.2.

Hence, in order for  $SFR_{\text{rec}}/SFR$  and  $M_{*,\text{rec}}/M_*$  computed from EAGLE to be reliable predictions, it is important that the simulation reproduces the observed galaxy metallicities. Fig. 13 of S15 shows a comparison between the mass-metallicity relations for ISM gas and stars as predicted by EAGLE and various observational data sets. In general, the systematic uncertainties in the observations are large, mainly due to the uncertain calibration of the diagnostics, leading to significant offsets between different data sets, which generally decrease with increasing galaxy stellar mass. For  $M_* \gtrsim 10^{9.5} M_{\odot}$ , the fiducial *Ref-L100N1504* simulation agrees



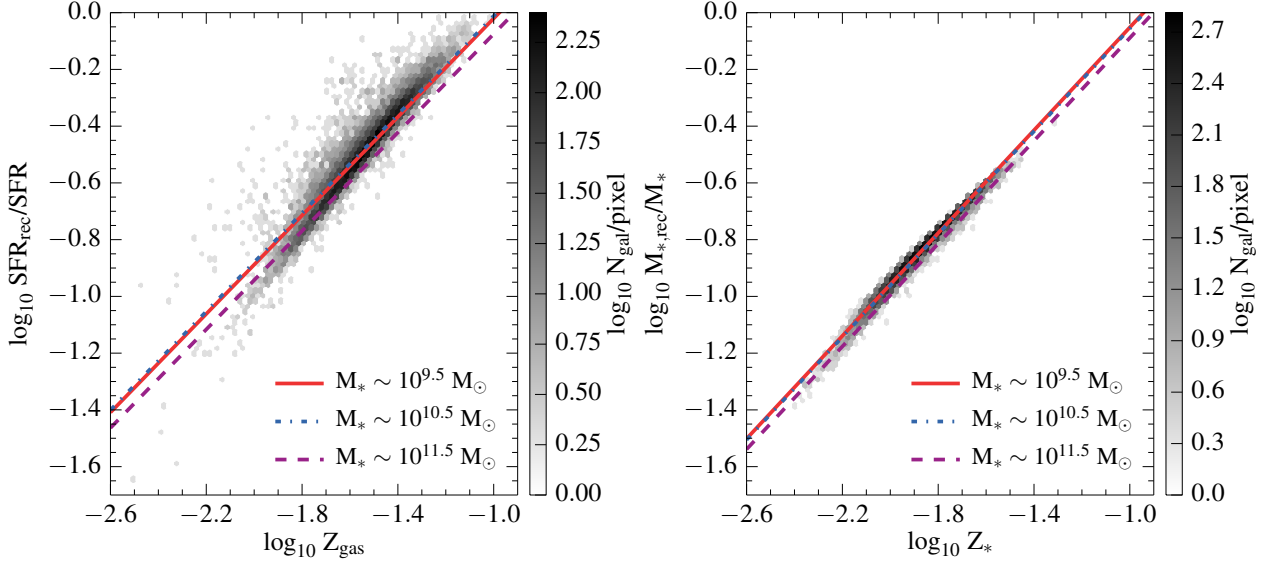


**Figure 4.** The fractional contribution of recycled stellar mass loss to the SFR (left) and stellar mass (right) of central galaxies at  $z = 0$  as a function of their average ISM and stellar metallicity, respectively. The grey scale indicates the number of galaxies in each cell, where we only include galaxies with stellar masses corresponding to at least 100 gas particles. In the left panel we only consider subhaloes with a non-zero SFR. We find tight power-law relations between the recycled gas contributions and the respective metallicity measures. These relations exhibit a slight mass dependence as a result of the increasing contribution from massive stars relative to intermediate-mass stars to the SFR and stellar mass for  $M_* \gtrsim 10^{10.5} M_\odot$ . The best-fit relations (equations 8 and 9), plotted for galaxies with  $M_* \sim 10^{9.5} M_\odot$  (red, solid line),  $M_* \sim 10^{10.5} M_\odot$  (blue, dot-dashed line) and  $M_* \sim 10^{11.5} M_\odot$  (purple, dashed line), serve as connections between the predictions for recycling-fuelled star formation given in this work and observational diagnostics and enable quantitative estimates of the SFR and stellar mass contributed by recycling from observed metallicities.

with the observed gas-phase metallicities from Zahid et al. (2014) to better than 0.1 dex and with Tremonti et al. (2004) to better than 0.2 dex. The *Recal-L025N0752* simulation predicts a somewhat steeper relation, with metallicities that are 0.1 dex lower at  $M_* \sim 10^{10} M_\odot$  and 0.2 dex lower at  $M_* \sim 10^9 M_\odot$  than those in the *Ref-L100N1504* simulation. While the observations from Tremonti et al. (2004) agree better with *Recal-L025N0752* over the whole mass range, the observations from Zahid et al. (2014) fall in between the two EAGLE models. The stellar metallicities predicted by *Ref-L100N1504* and *Recal-L025N0752* are converged for  $M_* \gtrsim 10^{10} M_\odot$ , where they agree with the observations from Galazzi et al. (2005) to better than 0.2 dex (and to better than 0.1 dex for  $M_* \gtrsim 10^{10.5} M_\odot$ ). At lower stellar mass, both EAGLE models are higher than the observations, with *Recal-L025N0752* being somewhat closer. However, considering the substantial uncertainty in the observations ( $> 0.5$  dex at  $M_* \sim 10^9 M_\odot$ ), they are still broadly consistent.

In Section 4.3.1 we will show that  $SFR_{\text{rec}}/SFR$  and  $M_{*,\text{rec}}/M_*$  vary as a function of galaxy mass in a way that is similar to  $Z_{\text{gas}}$  and  $Z_*$ . As expected, the level of agreement between *Ref-L100N1504* and *Recal-L025N0752* for the recycled gas contributions is also similar to that for the mass-metallicity relations.

However, there is an additional factor at play that may distort the one-to-one correspondence between the contribution of recycled gas to the SFR (and therefore to the stellar mass) and metallicity, namely the relative significance of the different mass loss channels. This depends on the timescale on which stars are formed, but is also affected by processes like stellar and AGN feedback. Given that the ejecta from massive stars have  $\sim 4 - 6$  times higher metallicity than those from intermediate-mass stars (dependent on metallicity; see Fig. 1), a higher contribution of the mass loss from

massive stars to the SFR (for fixed  $SFR_{\text{rec}}/SFR$ ) would yield a higher ISM metallicity, and would hence change the relation between  $SFR_{\text{rec}}/SFR$  and  $Z_{\text{gas}}$ . As we will show in Section 4.3.3, the contribution to the SFR of the mass loss from massive stars relative to that from AGB stars varies as a function of stellar mass, and in particular increases at the high-mass end. This introduces a mild mass dependence in the  $SFR_{\text{rec}}/SFR - Z_{\text{gas}}$  and  $M_{*,\text{rec}}/M_* - Z_*$  relations<sup>4</sup>. In order to relate this variation of the relative contribution from different mass loss channels to an observational diagnostic, we consider the average  $\alpha$ -enhancement,  $[\alpha/\text{Fe}]$ , represented by  $[\text{O}/\text{Fe}]$  (as oxygen dominates the  $\alpha$ -elements in terms of mass fraction), of ISM gas and stars. The fact that  $\alpha$ -elements are predominantly synthesized in massive stars, whereas of iron  $\sim 50\%$  is contributed by intermediate-mass stars in the form of SN Type Ia explosions and winds from AGB stars (e.g. Wiersma et al. 2009b), makes  $[\alpha/\text{Fe}]$  a good tracer for the relative importance of massive stars.

Adopting the usual definition of the abundance ratio,

$$\left[ \frac{\text{O}}{\text{Fe}} \right] = \log_{10} \left( \frac{X^{\text{O}}}{X^{\text{Fe}}} \right) - \log_{10} \left( \frac{X_{\odot}^{\text{O}}}{X_{\odot}^{\text{Fe}}} \right), \quad (7)$$

where  $X^x$  is the mass fraction of element  $x$  and  $X_{\odot}^{\text{O}}/X_{\odot}^{\text{Fe}} = 4.44$  is the solar abundance ratio (Asplund et al. 2009), we show  $[\text{O}/\text{Fe}]$

<sup>4</sup> Another factor is that the metal yields depend on metallicity (Fig. 1). This can change the  $SFR_{\text{rec}}/SFR - Z_{\text{gas}}$  and  $M_{*,\text{rec}}/M_* - Z_*$  relations even if the contributions from the different channels remain fixed. However, even a factor of 100 variation in the metallicity changes the metallicity of the stellar ejecta by only a few percent, which is significantly smaller than the effect of the change in the relative channel contributions in massive galaxies.

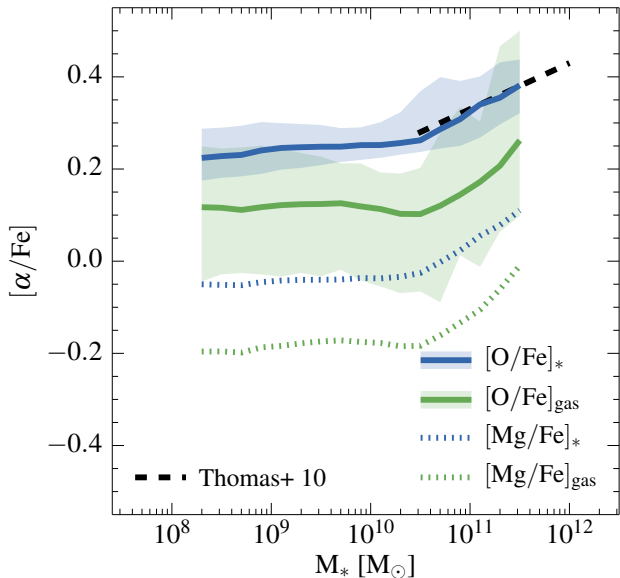


**Figure 5.** The  $\alpha$ -element-to-iron abundance ratio of central galaxies at  $z = 0$  as a function of stellar mass. We show  $[\alpha/\text{Fe}]$ , represented by  $[\text{O}/\text{Fe}]$  (solid) and  $[\text{Mg}/\text{Fe}]$  (dotted), of ISM gas (green) and stars (blue) as predicted by EAGLE, and compare with observations of the stellar  $[\alpha/\text{Fe}]$  from Thomas et al. (2010) (converted to a solar abundance ratio of  $X_{\text{O}}^{\text{O}}/X_{\text{O}}^{\text{Fe}} = 4.44$ ). The curves show the median value in each logarithmic mass bin of size 0.2 dex, if it contains at least 10 haloes and the stellar mass corresponds to at least 100 gas particles. The shaded regions mark the 10th to 90th percentiles, shown only for  $[\text{O}/\text{Fe}]$ . For  $M_* \lesssim 10^{10.5} M_{\odot}$ ,  $[\text{O}/\text{Fe}]$  ( $[\text{Mg}/\text{Fe}]$ ) is approximately constant at  $\sim 0.1$  ( $-0.2$ ) for gas and at  $0.25$  ( $-0.05$ ) for stars. For  $M_* \gtrsim 10^{10.5} M_{\odot}$ ,  $[\text{O}/\text{Fe}]$  and  $[\text{Mg}/\text{Fe}]$  increase with stellar mass, in such a way that the slope matches the observations, reflecting the enhancement in the contribution to the SFR and stellar mass from massive stars relative to that from intermediate-mass stars.

as a function of stellar mass in Fig. 5. The curves show the median in logarithmic mass bins of size 0.2 dex that contain at least 10 haloes and correspond to a stellar mass of at least 100 gas particles. The shaded regions mark the 10th to 90th percentile ranges. In both the gas-phase (green, solid) and the stellar phase (blue, solid),  $[\text{O}/\text{Fe}]$  is approximately constant at  $\sim 0.1$  and  $\sim 0.25$ , respectively, for  $M_* \lesssim 10^{10.5} M_{\odot}$ , but increases with stellar mass for  $M_* \gtrsim 10^{10.5} M_{\odot}$ . Comparing this to observations of the stellar  $[\alpha/\text{Fe}]$  for a sample of 3360 early-type galaxies from Thomas et al. (2010) (best-fit relation, after correcting for the difference in the set of solar abundances used; black dashed line), we find excellent agreement in terms of the slope and the normalization. While this is encouraging, suggesting that we capture the right mass dependence in the  $SFR_{\text{rec}}/SFR$ - $Z_{\text{gas}}$  and  $M_{*,\text{rec}}/M_*$ - $Z_*$  relations and that the cooling rates (which are dominated by oxygen at  $T \sim 2 \times 10^5$  K and by iron at  $T \sim 10^6$  K; see Wiersma et al. 2009a) employed by the simulation are realistic, the predicted abundance ratio is uncertain by a factor of  $> 2$  due to uncertainties in the nucleosynthetic yields and SN Type Ia rate (Wiersma et al. 2009b). It is therefore somewhat surprising that the agreement in the normalization is this good. If we consider  $[\text{Mg}/\text{Fe}]$ , which is another indicator of  $[\alpha/\text{Fe}]$  often used in the literature, of ISM gas (blue, dotted) and stars (green, dotted), we find an offset of  $\sim 0.3$  dex with respect to the observed  $[\alpha/\text{Fe}]$ . Note that the size of this offset is dependent on the adopted set of solar abundances. The slope, on the other hand, still matches the observed one, implying that the offset can

be attributed to a constant uncertainty factor in the (massive star) yields.

Motivated by the tight power-law relations shown in Fig. 4, we fit the relation between the recycled gas contribution to the SFR and ISM metallicity with the following function, including a term describing the variation in the relative channel contributions:

$$\log_{10} \frac{SFR_{\text{rec}}}{SFR} = 0.87 \log_{10} Z_{\text{gas}} - 0.40 \left[ \frac{\text{O}}{\text{Fe}} \right]_{\text{gas}} + 0.90, \quad (8)$$

where the values of the three free parameters have been obtained using least square fitting. Note that the metallicity  $Z$  is the average mass fraction of metals and is thus independent of the adopted solar value. Similarly, we determine the best-fit relation between the recycled gas contribution to the stellar mass and stellar metallicity:

$$\log_{10} \frac{M_{*,\text{rec}}}{M_*} = 0.91 \log_{10} Z_* - 0.28 \left[ \frac{\text{O}}{\text{Fe}} \right]_* + 0.92. \quad (9)$$

We show these relations in Fig. 4 for galaxies with  $M_* \sim 10^{9.5} M_{\odot}$  (red, solid line),  $M_* \sim 10^{10.5} M_{\odot}$  (blue, dot-dashed line) and  $M_* \sim 10^{11.5} M_{\odot}$  (purple, dashed line), where we use the median values of  $[\alpha/\text{Fe}]_{\text{gas}}$  and  $[\alpha/\text{Fe}]_*$  in stellar mass bins of 0.2 dex centred on the respective masses. As expected from Fig. 5, the relations at  $M_* \sim 10^{9.5} M_{\odot}$  and  $M_* \sim 10^{10.5} M_{\odot}$  are consistent, as a result of the median  $[\alpha/\text{Fe}]$  (of gas and stars) being constant for  $M_* \lesssim 10^{10.5} M_{\odot}$ . On the other hand, galaxies with  $M_* \sim 10^{11.5} M_{\odot}$  have  $SFR_{\text{rec}}/SFR$  and  $M_{*,\text{rec}}/M_*$  that are  $\sim 0.06$  and  $\sim 0.04$  dex lower at fixed metallicity due to an enhancement in the contribution from massive stars relative to that from intermediate-mass stars (reflected by their enhanced  $[\alpha/\text{Fe}]$  abundance ratio). These offsets are somewhat larger than the  $1\sigma$  scatter in the relation for all galaxy masses (which is set by the scatter at  $M_* < 10^{10} M_{\odot}$ ), indicating that the variation of the channel contributions at  $M_* > 10^{10.5} M_{\odot}$  significantly impacts upon the relation between metallicity and recycling-fuelled star formation in high-mass galaxies. It leads to a reduction of  $SFR_{\text{rec}}/SFR$  and  $M_{*,\text{rec}}/M_*$  at fixed metallicity that increases with stellar mass, and will therefore make any turnover or flattening at the high-mass end of the relation between recycled gas contributions and stellar mass (as seen in the mass-metallicity relation; see Tremonti et al. 2004; Gallazzi et al. 2005; Kewley & Ellison 2008; Andrews & Martini 2013; Zahid et al. 2014) more pronounced.

The fitting functions given in equations (8) and (9) serve as a crucial connection between the importance of gas recycling and observational diagnostics. To illustrate the usefulness of these relations, we will show in Section 4.3  $SFR_{\text{rec}}/SFR$  and  $M_{*,\text{rec}}/M_*$  as a function of stellar mass as ‘predicted’ by the observations by Zahid et al. (2014) and Gallazzi et al. (2005), where we convert the observed metallicities using equations (8) and (9). We then compare them to  $SFR_{\text{rec}}/SFR$  and  $M_{*,\text{rec}}/M_*$  directly computed from EAGLE. The results are generally in good agreement, particularly for  $M_* \gtrsim 10^{10} M_{\odot}$ , where EAGLE reproduces the observed mass-metallicity relation.

We note that the parameters of equations (8) and (9) are insensitive to the specific implementation of subgrid processes like star formation, stellar feedback and AGN feedback<sup>5</sup>, as for EAGLE changing their implementation affects the recycled gas contributions and metallicities in a similar way. Note that this may not

<sup>5</sup> The adopted IMF is an exception, as it determines the mass and metallicity of gas returned by stellar populations, as well as the relative contribution from massive stars with respect to intermediate-mass stars.

be true if the metallicity of galactic winds differs significantly from the metallicity of the ISM, as might for example happen if metals are preferentially ejected (e.g. Mac Low & Ferrara 1999; Creasey et al. 2015).

Recall that the subgrid parameters for stellar and AGN feedback in the *Recal-L025N0752* model have been recalibrated, in order to compensate for the increased numerical radiative losses in the higher-density gas that is resolved in the high-resolution simulation. The fact that the relations in Fig. 4 are converged (Appendix B2) with respect to the numerical resolution, indicates that any difference in  $SFR_{\text{rec}}/SFR$  and  $M_{*,\text{rec}}/M_*$  between *Ref-L100N1504* and *Recal-L025N0752*, which varies as a function of stellar mass (Fig. 6), is reflected by a similar difference in the gas-phase and stellar metallicities (fig. 13 in S15). Furthermore, the dependence on stellar mass of the  $SFR_{\text{rec}}/SFR$ - $Z_{\text{gas}}$  and  $M_{*,\text{rec}}/M_*$ - $Z_*$  relations only becomes significant for  $M_* \gtrsim 10^{10.5} M_{\odot}$ , which is the regime where *Ref-L100N1504* and *Recal-L025N0752* are converged (in terms of  $M_{*,\text{rec}}/M_*$  and  $Z_*$ ) or at least broadly consistent (in terms of  $SFR_{\text{rec}}/SFR$  and  $Z_{\text{gas}}$ ). As a final check, we explicitly calculate  $SFR_{\text{rec}}/SFR$  and  $M_{*,\text{rec}}/M_*$  as a function of stellar mass as predicted from the observed gas-phase and stellar metallicities, where we convert the metallicity using the equivalents of equations (8) and (9) from *Recal-L025N0752* (i.e. also using the values of  $[O/Fe]$  from that simulation), and find agreement with the results from *Ref-L100N1504* to better than a factor of  $\sim 1.07$  (0.03 dex). Therefore, we conclude that equations (8) and (9) are insensitive to an improvement of the resolution and corresponding recalibration of the subgrid physics, which means they can be considered numerically converged.

### 4.3 Dependence on halo and galaxy mass at $z = 0$

In this section we investigate how the fractional contribution of recycled gas to the present-day SFR and stellar mass of galaxies depends on their halo and stellar mass. Note that, because of the tight relation with metallicity that we established in Section 4.2, many conclusions that we draw here carry over to the mass-metallicity relation. We study both central and satellite galaxies and, in addition to the total contribution of gas recycling, assess the relative significance of the different mass loss channels. We also briefly explore how fuelling by gas recycling depends on the distance from the galactic centre. While we mainly present results from our fiducial *Ref-L100N1504* simulation, we start by comparing the results for central galaxies between the *Ref-L100N1504* and *Recal-L025N0752* simulations.

#### 4.3.1 Gas recycling in central galaxies

Fig. 6 shows the contribution of recycled stellar mass loss to the present-day SFR and stellar mass of central galaxies as a function of their mass in the *Ref-L100N1504* (red) and *Recal-L025N0752* (purple) simulations. We plot  $SFR_{\text{rec}}/SFR$  in the top row and  $M_{*,\text{rec}}/M_*$  in the bottom row as a function of subhalo mass (left column) and stellar mass (right column). For both simulations, the general trend in all four panels is that, at masses  $M_{\text{sub}} \lesssim 10^{12.2} M_{\odot}$  or  $M_* \lesssim 10^{10.5} M_{\odot}$ , the fraction of the SFR and stellar mass contributed by recycling increases with mass. This is the regime where stellar feedback becomes less efficient towards higher masses, since the greater depth of the gravitational potential well, as well as the higher pressure and density of the ISM and CGM, make it harder for feedback (dominated by star formation)

to eject gas from the galaxy and hence for recycled gas to be removed from the ISM. This leads to an increase of the values of  $SFR_{\text{rec}}/SFR$  and  $M_{*,\text{rec}}/M_*$  with mass.

The *Ref-L100N1504* and *Recal-L025N0752* yield similar trends, but they differ quantitatively by a factor of  $\sim 2$  (0.3 dex) in  $SFR_{\text{rec}}/SFR$  and  $M_{*,\text{rec}}/M_*$  at  $M_* \sim 10^9 M_{\odot}$  ( $M_{\text{sub}} \sim 10^{11} M_{\odot}$ ). This difference decreases towards higher masses, where for  $M_* \gtrsim 10^{9.8} M_{\odot}$  ( $M_{\text{sub}} \gtrsim 10^{11.6} M_{\odot}$ ), *Ref-L100N1504* and *Recal-L025N0752* are converged in terms of  $M_{*,\text{rec}}/M_*$  and broadly consistent in terms of  $SFR_{\text{rec}}/SFR$  (considering the substantial amount of scatter and relatively poor sampling in the *Recal-L025N0752* model). The divergence at lower masses is not surprising considering the difference between the two models in terms of their specific SFR ( $= SFR/M_*$ , sSFR; see fig. 11 of S15) and metallicity (fig. 13 of S15), both of which are closely related to  $SFR_{\text{rec}}/SFR$  and  $M_{*,\text{rec}}/M_*$  (as discussed in Sections 4.3.2 and 4.2). S15 showed that the *Recal-L025N0752* model, which drives stronger outflows, is in slightly better agreement with the observed sSFR and metallicity at these mass scales. We therefore conclude that at  $M_* \lesssim 10^{9.8} M_{\odot}$  the values of  $SFR_{\text{rec}}/SFR$  and  $M_{*,\text{rec}}/M_*$  predicted by the *Recal-L025N0752* model are more reliable than those predicted by the fiducial model, whereas at higher mass, where the two models converge, the fiducial model (with a 64 times larger volume) provides a better sampling of the galaxy population and therefore a more reliable estimate of the median  $SFR_{\text{rec}}/SFR$  and  $M_{*,\text{rec}}/M_*$ . To limit the number of model curves plotted in each figure, from now on we will only plot the results from the fiducial EAGLE simulation and ask the reader to keep in mind the slight overprediction of the recycled gas contribution to the SFR and stellar mass of galaxies with  $M_* \lesssim 10^{9.8} M_{\odot}$ .

At the high-mass end in Fig. 6 (as shown by the *Ref-L100N1504* simulation), galaxies with  $M_* \gtrsim 10^{10.5} M_{\odot}$  ( $M_{\text{sub}} \gtrsim 10^{12.2} M_{\odot}$ ) show a different trend than at lower masses. Due to the feedback from AGN, which becomes stronger in more massive systems,  $SFR_{\text{rec}}/SFR$  and  $M_{*,\text{rec}}/M_*$  turn over at  $M_* \sim 10^{10.5} M_{\odot}$ , then decrease and remain constant, respectively, at higher masses. Note that even though this type of feedback is not associated with any replenishment of the ISM gas reservoir (as opposed to feedback from star formation, which directly provides the gas for recycling), it does have a significant impact on the rate at which galaxies consume the enriched ISM gas. If AGN are efficient at launching galactic outflows, which is only the case in massive galaxies, they preferentially remove or disperse the dense ISM gas from the central regions, in which the abundance of stellar ejecta is high. Hence, efficient AGN feedback reduces  $SFR_{\text{rec}}/SFR$  and  $M_{*,\text{rec}}/M_*$  and regulates the turnover at  $M_* \sim 10^{10.5} M_{\odot}$ .

We note that while the use of the 30 kpc 3D aperture has a negligible effect on the total SFR, it does somewhat enhance  $SFR_{\text{rec}}/SFR$  for galaxies with  $M_* \gtrsim 10^{10.5} M_{\odot}$ . This is consistent with the fraction of the SFR fuelled by recycled gas being larger in the inner parts (see Fig. 10). Similarly,  $M_{*,\text{rec}}/M_*$  is somewhat enhanced if an aperture is applied. In Appendix C we show that the effect of using an aperture is that the slopes of  $SFR_{\text{rec}}/SFR$  and  $M_{*,\text{rec}}/M_*$  at  $M_* \gtrsim 10^{10.5} M_{\odot}$  ( $M_{\text{sub}} \gtrsim 10^{12.2} M_{\odot}$ ) become shallower. Without an aperture,  $M_{*,\text{rec}}/M_*$  decreases with halo and galaxy mass (similar to  $SFR_{\text{rec}}/SFR$ ), instead of remaining roughly constant if an aperture is applied. Hence, while the turnover is regulated by the efficiency of AGN feedback, the use of an aperture also plays a role in shaping the behaviour of  $SFR_{\text{rec}}/SFR$  and  $M_{*,\text{rec}}/M_*$  at the high-mass end.

At the mass scale of the turnover, the fractional contribution

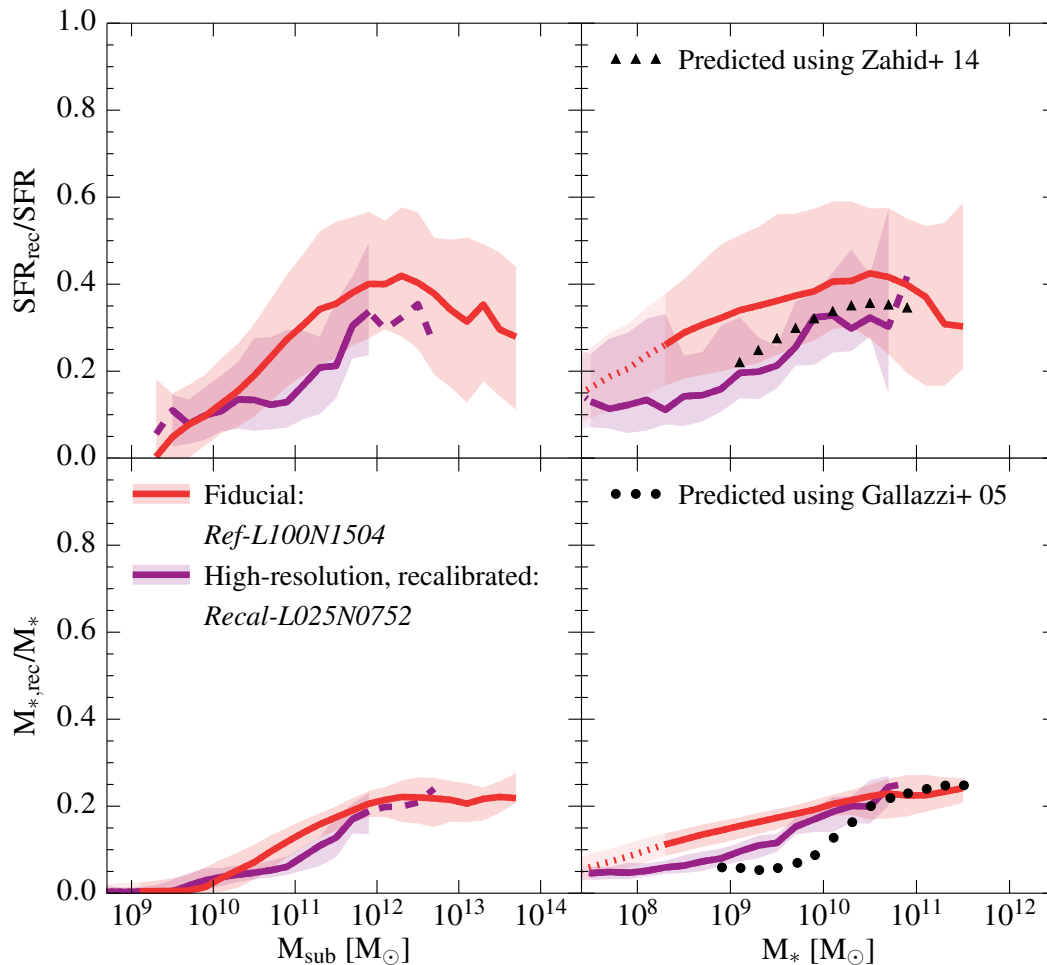


**Figure 6.** The fractional contribution of gas recycled from stellar mass loss to the SFR (top) and stellar mass (bottom) of central galaxies at  $z = 0$  as a function of their subhalo mass (left) and stellar mass (right). We show the results for the fiducial EAGLE model (*Ref-L100N1504*; red) and the high-resolution, recalibrated model (*Recal-L025N0752*; purple). We only consider subhaloes with a non-zero SFR (top panels) or a non-zero stellar mass (bottom panels). The curves show the median value in each logarithmic mass bin of size 0.2 dex, if it contains at least 10 galaxies. The shaded regions mark the 10th to 90th percentile ranges. The solid curves become dotted when the subhalo (stellar) mass corresponds to fewer than 100 DM (baryonic) particles and become dashed (for *Recal-L025N0752* only) when there are less than 10 haloes per bin. The contribution of recycled gas to the SFR and stellar mass first increases with mass, turns over at  $M_* \sim 10^{10.5} M_\odot$  ( $M_{\text{sub}} \sim 10^{12.2} M_\odot$ ), and then decreases or remains constant at higher mass. This trend is regulated by the efficiency of the feedback from star formation (AGN) at low (high) masses: galactic winds eject gas from the ISM, where stellar mass loss accumulates, and therefore preferentially reduce the SFR and stellar mass contributed by recycling. The black points represent our best estimate of the recycled gas contributions to the SFR and stellar mass (for a central galaxy with a Milky Way-like mass: 35% and 20%, respectively), calculated by applying equations (8) and (9) to the observed gas-phase metallicities from Zahid et al. (2014) and the observed stellar metallicities from Gallazzi et al. (2005). These estimates are in broad agreement with the predictions computed directly from EAGLE.

of recycled gas to the SFR is at a maximum. A galaxy of this mass,  $M_* \sim 10^{10.5} M_\odot$ , is too massive to have effective star formation-driven outflows but still too small for AGN feedback to be effective. Not surprisingly, this mass scale coincides with the peak in the galaxy formation efficiency (see fig. 8 of S15), which is consistent with the efficiency of feedback being the main driver of  $SFR_{\text{rec}}/SFR$  and  $M_{*,\text{rec}}/M_*$ . The fiducial EAGLE model indicates that for a Milky Way-like galaxy, which is at the peak of the galaxy formation efficiency, 40% of its present-day SFR and 20% of its present-day stellar mass is due to the recycling of stellar mass loss.

As the relation between  $SFR_{\text{rec}}/SFR$  ( $M_{*,\text{rec}}/M_*$ ) and stellar mass reflects the relation between ISM (stellar) metallicity and stellar mass (see Section 4.2), our investigation of the origin of

the former has direct implications for the origin of the latter. Our results imply that the increase in the mass-metallicity relation at  $M_* \lesssim 10^{10.5} M_\odot$  is due to the decreasing efficiency of stellar feedback at driving galactic outflows, while the shape at higher mass is governed by the efficiency of AGN feedback.

Finally, we provide a quantitative estimate of  $SFR_{\text{rec}}/SFR$  (triangular points, upper-right panel of Fig. 6) and  $M_{*,\text{rec}}/M_*$  (circular points, lower-right panel of Fig. 6) by applying the (numerically converged) relations given in equations (8) and (9) to the observed gas-phase metallicities from Zahid et al. (2014) and the observed stellar metallicities from Gallazzi et al. (2005), where we used the median [O/Fe] in each stellar mass bin. These estimates agree qualitatively with  $SFR_{\text{rec}}/SFR$  and  $M_{*,\text{rec}}/M_*$  computed directly from the fiducial EAGLE model, showing a steep increase

with mass for  $M_* \lesssim 10^{10.5} M_\odot$ , followed by turnover and even a slight downturn in  $SFR_{\text{rec}}/SFR$  at higher masses<sup>6</sup>. Quantitatively, the black points are in good agreement with the fiducial EAGLE model for  $M_* \gtrsim 10^{10} M_\odot$  and with *Recal-L025N0752* also at lower masses, as expected from the comparison of the mass-metallicity relation with the observations presented in S15. If the discrepancy between the predicted and observed mass-metallicity relation exceeds the systematic error due to calibration uncertainties in the observations, then the black points represent our best estimates of the recycled gas contributions to the SFR and stellar mass. For a Milky Way-like galaxy ( $M_* \sim 10^{10.5} M_\odot$ ), we find these contributions to be 35% and 20%, respectively.

#### 4.3.2 Gas recycling in satellite galaxies

Having studied the recycling-fuelled star formation in present-day central galaxies, we now compare these with the results for present-day satellite galaxies. Fig. 7 shows the SFR and stellar mass contributed by recycling for both central (red; as in Fig. 6) and satellite (blue) galaxies, as predicted by the fiducial *Ref-L100N1504* simulation. In general, these are broadly similar for centrals and satellites. However, we identify two important differences. Firstly, in the left panels, where we show the two ratios as a function of subhalo mass, the relations for satellite galaxies are shifted towards lower masses relative to those for central galaxies. Satellites lose a fraction of their dark matter subhalo mass (but less stellar mass) upon infall onto the larger-scale dark matter halo as a result of tidal stripping. Hence, this shift illustrates the fact that satellite galaxies live in smaller (sub)haloes than central galaxies of similar stellar mass. Secondly, in the top-right panel, at a mass scale of  $M_* \sim 10^{10.5} M_\odot$ , where  $SFR_{\text{rec}}/SFR$  reaches its maximum value, the satellite galaxies show substantial scatter towards a high recycled gas contribution. Both the median ( $\sim 50\%$ ) and 90th percentile ( $\sim 85\%$ ) values are significantly higher than for centrals. At lower and higher masses this difference is smaller. We therefore conclude that in the regime where both stellar feedback and AGN feedback are relatively inefficient, gas recycling plays a more important role in fuelling ongoing star formation in satellite galaxies than in central galaxies. For  $M_{*,\text{rec}}/M_*$ , on the other hand, there is no difference between centrals and satellites, because satellites formed nearly all their stars while they were still centrals.

To get a better understanding of the difference between centrals and satellites, we consider the relation between  $SFR_{\text{rec}}/SFR$  and sSFR. Fig. 8 shows this relation for centrals (upper panels) and satellites (lower panels) with masses  $10^{9.5} M_\odot < M_* < 10^{10.5} M_\odot$  (left) and  $10^{10.5} M_\odot < M_* < 10^{11.5} M_\odot$  (right), where the histograms at the top compare the distributions of sSFRs. In order to limit the dynamical range plotted, galaxies with  $SFR/M_* < 10^{-12} \text{ yr}^{-1}$  are shown as upper limits. The colour coding indicates the mass of the large-scale DM halo,  $M_{200}$ , in which these galaxies reside. For centrals,  $M_{200}$  is generally closely related to the mass of the subhalo and the stellar mass, whereas for satellites the mass of the host halo they have fallen onto is only weakly related to their own mass. For satellites,  $M_{200}$  instead serves as a proxy for the

strength of any environmental effects like ram-pressure stripping (Gunn & Gott 1972) or strangulation (Larson et al. 1980).

Focusing first on the centrals in the lower stellar mass bin, we see a clear anticorrelation between the fraction of the SFR that is fuelled by recycling and the sSFR. This can be explained by the fact that sSFR is closely related to the gas fraction ( $= M_{\text{gas}}/(M_{\text{gas}} + M_*)$  with  $M_{\text{gas}}$  the ISM mass): higher gas fractions generally correspond to higher sSFRs. Also, since the ISM is comprised of both processed and unprocessed gas, whereas stellar mass only provides enriched gas for recycling, an enhanced gas fraction typically implies that a greater fraction of the star formation in the ISM is fuelled by unprocessed, ‘nonrecycled’ gas (i.e.  $SFR_{\text{rec}}/SFR$  is low). On the other hand, galaxies with a low sSFR and a correspondingly low gas fraction will have a higher fraction of their SFR contributed by recycling. Considering the centrals in the higher mass bin, we see that while part of this relation is still in place, a significant fraction lies away from the main relation towards the lower left. This is the result of efficient AGN feedback, which suppresses both the sSFR (‘quenching’) and the  $SFR_{\text{rec}}/SFR$  of galaxies, as AGN feedback is more important at higher halo masses. This explanation is consistent with the enhanced halo masses of the galaxies in this regime ( $M_{200} \sim 10^{13} M_\odot$  for centrals with  $SFR/M_* \sim 10^{-11.5}$  and  $SFR_{\text{rec}}/SFR \sim 0.2$ , compared to  $M_{200} \sim 10^{12} M_\odot$  for centrals with  $SFR/M_* \sim 10^{-10.5} \text{ yr}^{-1}$  and  $SFR_{\text{rec}}/SFR \sim 0.5$ ). At even higher central galaxy mass scales than shown in Fig. 8, the anticorrelation between sSFR and  $SFR_{\text{rec}}/SFR$  disappears entirely. Instead, the relation transforms into an AGN feedback-controlled correlation (although weak due to small number statistics, with a Pearson correlation coefficient of 0.43 for  $M_* > 10^{11.0} M_\odot$ ), such that the galaxies with the lowest sSFRs have the lowest recycling-fuelled SFRs.

Having investigated the mechanism driving the sSFR -  $SFR_{\text{rec}}/SFR$  trends in the two mass regimes for centrals, we now consider satellites. In the lower mass bin the anticorrelation between sSFR and  $SFR_{\text{rec}}/SFR$  is similar to that for centrals, although the histogram at the top shows that the sSFR distribution for satellites has larger scatter towards low sSFRs. As previously discussed, low sSFRs are related to low ISM gas fractions and result in high fractions of the SFR contributed by recycling. We indeed see a population of satellite galaxies at  $SFR/M_* \sim 10^{-11} \text{ yr}^{-1}$  with fractional contributions of recycled gas to their SFR as high as 90–95%. This high- $SFR_{\text{rec}}/SFR$  regime is more frequently populated by satellites than similarly massive centrals, reflecting the substantially greater scatter in the satellite curves towards high values of  $SFR_{\text{rec}}/SFR$  at  $M_* \sim 10^{10.5}$  seen in Fig. 7. As indicated by the colour coding in Fig. 8, this population of satellites is hosted by relatively massive group-scale DM haloes ( $M_{200} \sim 10^{14} M_\odot$ ), implying that their low sSFRs and gas fractions are the result of the cessation of fresh gas infall (either because cooling is inefficient or because the satellite’s hot gas reservoir was stripped), and/or a (partial) removal of cold gas from the disc. Both scenarios lead to a depletion of the ISM gas reservoir and a greater dependence on stellar mass loss for replenishing it.

Finally, we focus on the satellite galaxies in the higher mass bin, shown in the bottom-right of Fig. 8. Whereas most similarly massive central galaxies that have moved away from the sSFR -  $SFR_{\text{rec}}/SFR$  anticorrelation, have moved towards low sSFR and low  $SFR_{\text{rec}}/SFR$  under the influence of AGN feedback, there is still a significant population of satellite galaxies occupying the high- $SFR_{\text{rec}}/SFR$  region. Inspecting the masses of the BHs residing in these satellites (not shown) we see that they are significantly lower than the masses of BHs in centrals of similar stellar mass.

<sup>6</sup> Note that, even though the mass-metallicity relation observed by Zahid et al. (2014) does not exhibit a decrease in the metallicity at the high-mass end, the recycled gas contribution to the SFR can still show a slight downturn, due to the change in the relative contributions from the different mass loss channels (as discussed in Section 4.2).

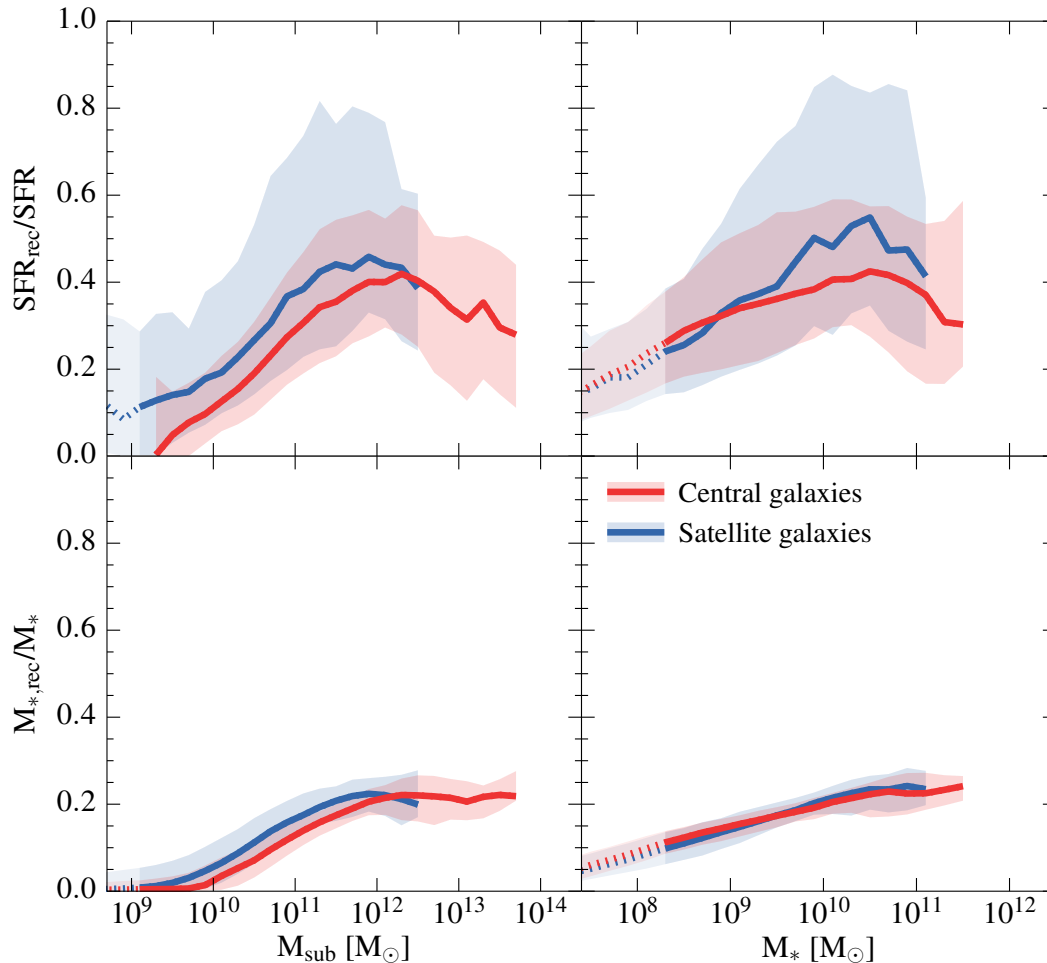


**Figure 7.** As Fig. 6, but showing the results for central (red) and satellite (blue) galaxies from the fiducial EAGLE model. The recycled gas contributions to the SFR and stellar mass in satellites are broadly consistent with the ones in similarly massive centrals, since the efficiency of stellar and AGN feedback is the controlling factor in fuelling star formation with recycled gas. However, in the inefficient feedback regime ( $M_* \lesssim 10^{10.5} M_\odot$ ), satellites with low gas fractions can reach recycling-fuelled SFR fractions as high as  $\sim 90\%$ , with a median that exceeds the one in similarly massive centrals (see also Fig. 8).

We infer that this is again due to the depletion of the satellite ISM gas, thereby preventing efficient BH growth. This explains why the AGN feedback in these satellites is unable to suppress the recycled gas contribution to the SFR.

We conclude that the SFR and stellar mass contributed by recycling are broadly consistent between central and satellite galaxies over a wide range of galaxy masses, because gas recycling is governed primarily by the efficiency of stellar and AGN feedback. However, in satellites with a stellar mass similar to that of the Milky Way, the mass scale at which feedback is least efficient at suppressing star formation, the recycled gas contribution to the SFR often exceeds the one in similarly massive centrals (and can even reach  $\gtrsim 90\%$ ), as the depletion of their ISM gas reservoir makes them more reliant on stellar mass loss for fuelling ongoing star formation.

Our findings are consistent with the observational inference that, at a given stellar mass, satellites are more metal-rich than centrals (Pasquali et al. 2012; Peng & Maiolino 2014). We explain the origin of their different mass-metallicity relation as a consequence of satellites being subject to environmental processes like

ram-pressure stripping and strangulation, which prevent the dilution of the ISM reservoir by metal-poor gas.

#### 4.3.3 Contributions from AGB stars, SN Type Ia and massive stars

To assess the relative significance of the different stellar mass loss channels for fuelling star formation in present-day centrals and satellites, we show in Fig. 9 the contribution of recycled gas to the SFR (top panels) and stellar mass (bottom panels) split into the contributions from AGB stars (blue), massive stars (purple) and SN Type Ia (cyan). These are plotted as a function of galaxy stellar mass for centrals (left panels) and satellites (right panels) at  $z = 0$ .

From the top panels, we see that AGB stars are of greater importance for fuelling present-day star formation than massive stars in all but the most massive central galaxies. Up to 24% (32%) of the SFR in centrals (satellites) is fuelled by gas recycled from AGB stars, while  $\lesssim 17\%$  ( $\lesssim 20\%$ ) is fuelled by gas from massive stars. Integrated over cosmic history (as quantified by  $M_{*,\text{rec}}/M_*$  in the lower panels), their contributions are approximately equal at all but the highest mass scales. This may appear difficult to reconcile with

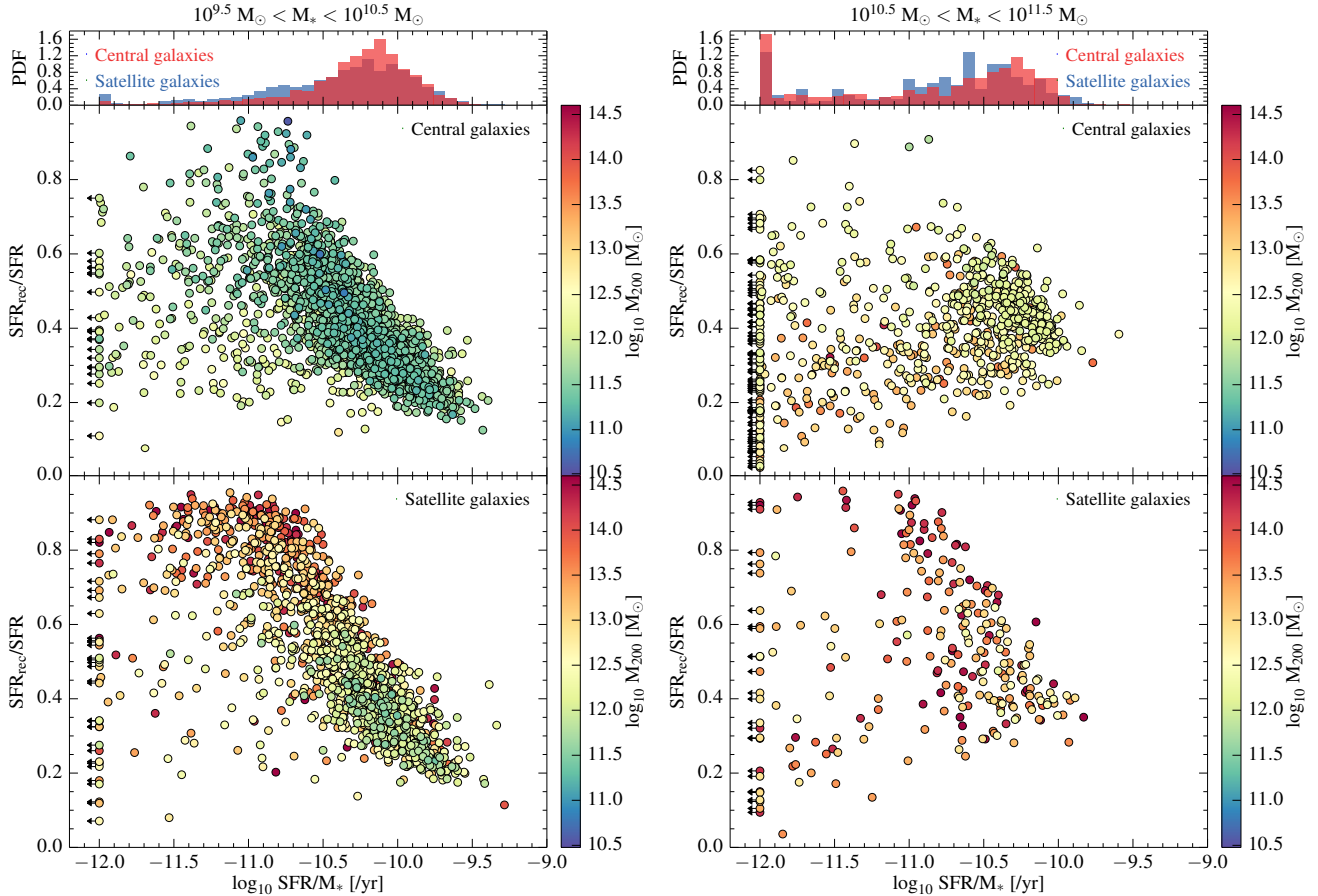


**Figure 8.** The SFR fuelled by recycling as a function of sSFR ( $= SFR/M_*$ ), colour-coded by host halo mass ( $M_{200}$ ), for central galaxies (upper panels) and satellite galaxies (lower panels) with stellar masses  $10^{9.5} M_{\odot} < M_* < 10^{10.5} M_{\odot}$  (left) and  $10^{10.5} M_{\odot} < M_* < 10^{11.5} M_{\odot}$  (right). The histograms at the top show the distributions of the sSFR for centrals and satellites in these two mass bins. Galaxies with  $SFR/M_* < 10^{-12} \text{ yr}^{-1}$  are shown as upper limits. For the centrals, the relation between the recycling-fuelled SFR and the sSFR changes from an anticorrelation at lower mass, which is a result of the tight relation with ISM gas fraction, to a (weak) correlation at higher mass, which is driven by AGN feedback. The satellites, on the other hand, show a similar behaviour, but retain in both mass ranges a large population of low-sSFR galaxies that rely heavily on stellar mass loss for fuelling ongoing star formation (contributing  $\gtrsim 90\%$ ).

the timed mass release from intermediate-mass and massive stars for a single SSP presented in Fig. 1, where we showed that massive stars are the dominant source of (integrated) mass loss for SSP ages  $\lesssim 1$  Gyr and that massive stars and AGB stars contribute about equally at higher ages. Fig. 9 implies that stellar ejecta do not simply accumulate in the ISM, but that they are removed, either by star formation or by outflows, in a way that affects the ejecta from AGB stars and massive stars differently<sup>7</sup>.

The ejecta from massive stars are released almost instantaneously compared to those from AGB stars (see Fig. 1). This means that, before AGB stars start to contribute significantly to the recycled gas, secondary generations of stars will already have formed from the massive star ejecta, causing an increasing fraction of these ejecta to become locked up in stellar remnants. While they then still contribute to the stellar mass of the galaxy, they no longer fuel

ongoing star formation. Furthermore, a considerable amount of gas from massive stars will already have been ejected in galactic winds, before the AGB stars shed most of their mass. As a result, the contribution from massive stars to the present-day SFR is suppressed compared to that from AGB stars.

In general, if stars are older, the surrounding gas will contain a higher fraction of ejecta from intermediate-mass stars than from massive stars. This means that, at fixed stellar mass, galaxies with a low SFR (which includes passive galaxies) are expected to contain enhanced fractions of AGB ejecta, as only newly formed stars produce massive star ejecta, while evolved, intermediate-mass stars still shed mass in AGB winds. Not surprisingly, we see that the scatter to high values of  $SFR_{\text{rec}}/SFR$  for satellites with masses  $10^{10} M_{\odot} < M_* < 10^{11} M_{\odot}$  (upper-right panel of Fig. 7) is mainly due to satellites with large fractions of the AGB ejecta being recycled, consistent with their low sSFRs (Fig. 8)<sup>8</sup>.

<sup>7</sup> As our findings in Sections 4.3.1 and 4.3.2 already imply, the relation between the mass loss from individual SSPs and the contribution of this mass loss to the SFR and stellar mass on galactic scales is not straightforward, since the rate of gas accretion and the efficiencies of stellar and AGN feedback depend on the mass of the galaxy.

<sup>8</sup> Despite the shallow, but significant, decrease in the sSFRs with mass of galaxies with  $M_* \lesssim 10^{10.5} M_{\odot}$  (shown in fig. 11 of S15), we do not see an increase in the  $SFR_{\text{rec}}/SFR$  from AGB stars relative to  $SFR_{\text{rec}}/SFR$  from massive stars in this mass range. Note that we are now considering the

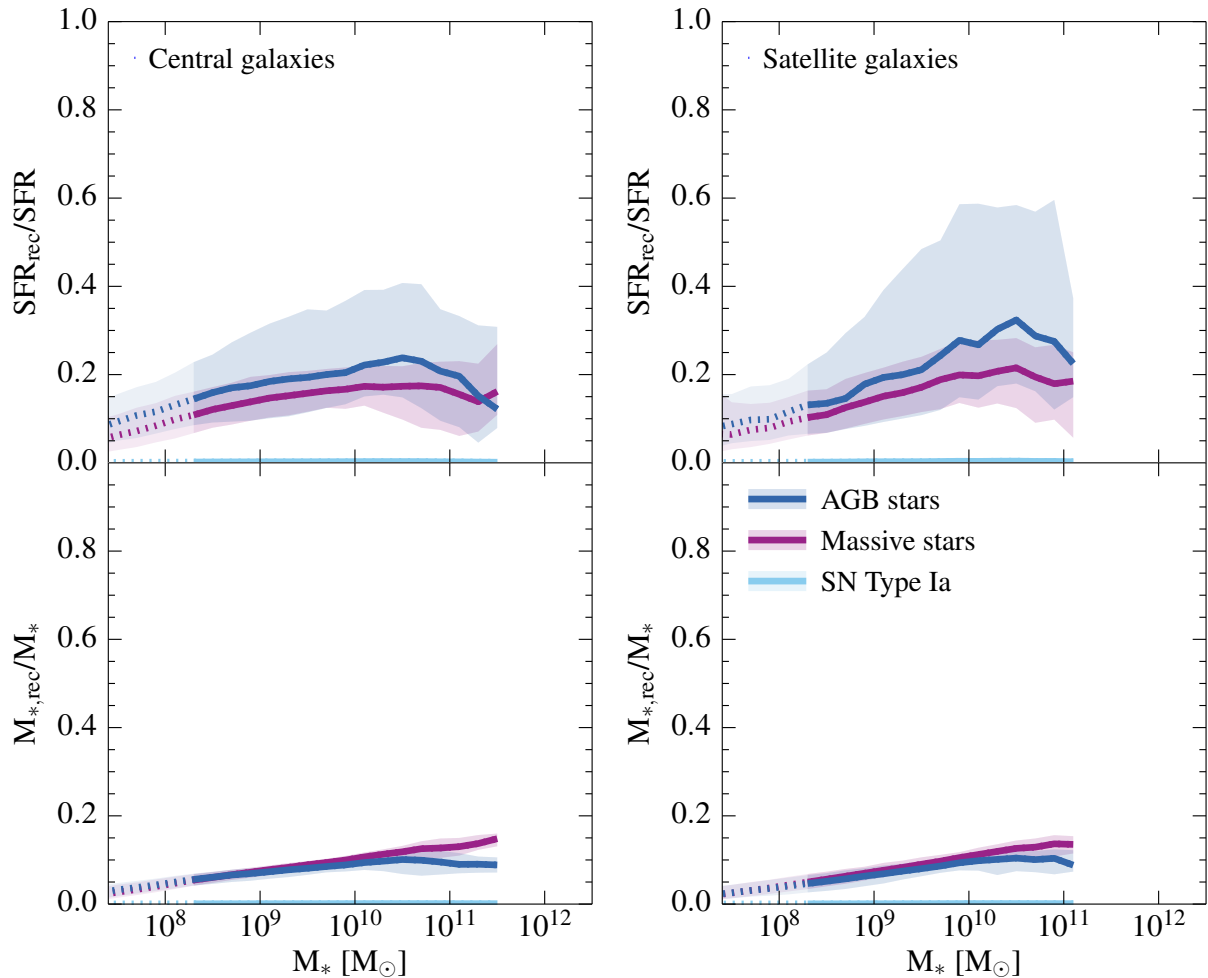


**Figure 9.** The contribution of gas from AGB stars (blue), massive stars (purple) and SN Type Ia (cyan) to the SFR (top) and stellar mass (bottom) of galaxies at  $z = 0$  as a function of their stellar mass. The results for centrals and satellites are shown in the left and right panels, respectively. The curves and shaded regions indicate the medians and 10th to 90th percentile ranges, as in Fig. 7. In general, the gas from AGB stars and massive stars contributes about equally to the SFR and stellar mass in both centrals and satellites. However, there is a slight enhancement in the contribution from AGB stars to the SFR at all but the highest mass scales, due to the preferential removal of massive star ejecta by star formation-driven winds and by lock up in stellar remnants. AGB ejecta are also responsible for the high  $SFR_{\text{rec}}/SFR$  values of some satellites, since these environmentally quenched objects have low sSFRs and cannot accrete gas. At the high-mass end, the relative contribution from AGB ejecta declines, because AGN feedback (which is unimportant at low mass) can drive them out even in the absence of star formation.

Finally, in massive galaxies ( $M_* \gtrsim 10^{10.5} M_\odot$ ), there is a decline of the  $SFR_{\text{rec}}/SFR$  and  $M_{*,\text{rec}}/M_*$  contributed by AGB stars, while the contributions from massive stars decrease only mildly (or flatten). This is consistent with the increase in the  $[O/Fe]$  abundance ratio, as shown in Fig. 5 of Section 4.2, where we discussed that this change in the relative significance of the different mass loss channels introduces a mass dependence in the relation between recycling-fuelled star formation and metallicity. We attribute this effect to ‘downsizing’, a scenario in which the bulk of the stars in more massive galaxies has formed earlier and over a shorter pe-

ratio of the blue and purple curves in the upper and lower left panels (focussing on central galaxies). Instead, the relative contribution from massive stars, both to the SFR (upper panels) and stellar mass (lower panels), remains approximately constant. This is due to a competing effect, namely the decrease in star formation feedback efficiency, which mitigates the preferential expulsion of massive star ejecta.

riod of time than in lower-mass counterparts (e.g. Cowie et al. 1996; Neistein et al. 2006; Cattaneo et al. 2008; Fontanot et al. 2009).

The rapid and efficient star formation in the progenitors of present-day massive galaxies is however suppressed at later times, when these progenitors have grown massive enough for AGN feedback to become efficient and the gas cooling rates to drop. Moreover, while winds driven by feedback from star formation will not be available to drive out AGB ejecta in quenched galaxies, AGN feedback can. Hence, this scenario is consistent with the reduction in the contribution from AGB stars, relative to that from massive stars, to both the SFR (upper panels) and the stellar mass (lower panels) at the highest mass scales shown in Fig. 9.

We infer that galaxies generally obtain most of their metals from massive star ejecta, as these ejecta have 4 – 6 times higher metallicity than those from AGB stars, while the fraction of the (total) ISM mass and stellar mass contributed by massive star ejecta is similar to that contributed by AGB ejecta. This holds for met-



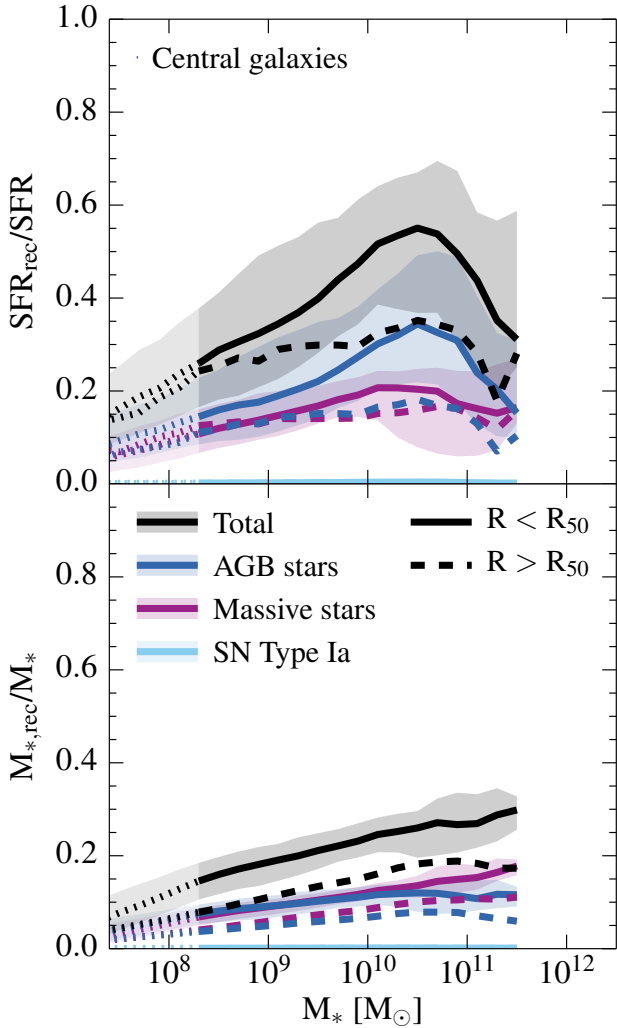


**Figure 10.** As the left column of Fig. 9, but split into gas and stars inside the stellar half-mass radius  $R_{50}$  (solid) and outside  $R_{50}$  (dashed). The 10th to 90th percentile ranges are only shown for inside  $R_{50}$ . Gas recycling is more important for fuelling star formation (at the present-day and in the past) in the inner parts of galaxies than in the outskirts. Consistent with inside-out growth, the gas in the central regions is comprised of an enhanced fraction of AGB ejecta, which is the main driver of the greater contribution of gas recycling to the star formation within  $R_{50}$ .

als in the gas-phase, but even more so for metals in the stellar phase. In both cases, the metal content contributed by massive star ejecta increases at the high-mass end ( $M_* \gtrsim 10^{10.5} M_\odot$ ) of the mass-metallicity relation, as reflected by the variation in the  $[O/Fe]$  abundance ratio (Fig. 5).

#### 4.3.4 Radial dependence of gas recycling

Having explored the importance of gas recycling on galaxy-wide scales, we now briefly investigate how the significance of recycling for fuelling star formation depends on the distance from the galactic centre. In Fig. 10 we plot, similar to the left column of Fig. 9, the contribution of gas from AGB stars (blue), massive stars (purple) and SN Type Ia (cyan) to the SFR (top) and stellar mass (bottom) of centrals at  $z = 0$ , now separated into gas and stars inside (solid

lines) and outside (dashed lines) the stellar half-mass radius. This radius, denoted by  $R_{50}$ , is the 3D radius that encloses 50% of the stellar mass bound to the subhalo (within the 30 pkpc 3D aperture). It is typically  $\sim 4$  pkpc for a  $M_* \sim 10^{10} M_\odot$  galaxy. Note that we split both the numerator and the denominator of  $SFR_{rec}/SFR$  and  $M_{*,rec}/M_*$  into  $R < R_{50}$  and  $R > R_{50}$ . We also plot the total recycled gas contribution (black), which is the sum over the three stellar mass loss channels, to the SFR and stellar mass in these two radial regimes. For clarity, we only show the 10th to 90th percentile ranges for  $R < R_{50}$ .

Focusing first on the total (black lines), both panels consistently show that gas recycling is more important for fuelling star formation (at the present-day and in the past) in the central parts of galaxies than in the outskirts. This is consistent with observational inference that galaxies grow in an inside-out fashion (e.g. Muñoz-Mateos et al. 2007; Patel et al. 2013), with the oldest stars residing in the centre and the replenishment of the gas reservoir by late infall being primarily significant in the outskirts of the disc (owing to its relatively high angular momentum). From the black curves in the upper panel we see that, at the peak value, 55 – 60% of the SFR inside  $R_{50}$  is due to stellar mass loss, compared to only 35 – 40% outside  $R_{50}$ . As a result, also a higher fraction of the stellar mass inside  $R_{50}$  comes from recycling,  $\sim 30\%$  at the mass scale where recycling is most significant, compared to  $\sim 20\%$  in the outskirts.

To investigate what drives this radial dependence, we turn to the relative significance of the different sources of mass loss. While outside  $R_{50}$  AGB stars (blue, dashed) and massive stars (purple, dashed) contribute about equally to the SFR for all masses, inside  $R_{50}$  the contribution from AGB stars (blue, solid) is significantly larger than the contribution from massive stars (purple, solid). As discussed in the previous section, the gas around older stellar populations contains higher fractions of AGB ejecta. Hence, the difference between the inner and outer parts reflects the radial age gradient of the stars, due to the inside-out growth of the galaxy.

The drop in the AGB contribution at the high-mass end that we saw in Fig. 9, is present in both the inner and outer parts, but it is much stronger near the galactic centre. This is consistent with it being due to a lack of intermediate-age stars and the ability of AGN to drive out the AGB ejecta even in the absence of star formation.

The radial variation of  $SFR_{rec}/SFR$  and  $M_{*,rec}/M_*$  is consistent with the negative metallicity gradients observed in local disc galaxies (e.g. Zaritsky et al. 1994; Moustakas et al. 2010; Sánchez et al. 2014). Our results imply that, although the majority of the metals in galaxies (both in the ISM and stars) comes from massive star ejecta, the relative contribution from AGB ejecta is on average larger near the galactic centre than in the outskirts. This holds in particular for the ISM metal content of Milky Way-like ( $M_* \sim 10^{10.5} M_\odot$ ) galaxies.

## 5 EXPLORING MODEL VARIATIONS WITH OWLS

In this section we assess the sensitivity of our results from the EAGLE simulation presented in Section 4 to the physical processes included in the subgrid model. We do this by comparing the outcomes of a set of simulations in which the subgrid model is systematically varied. We focus particularly on the feedback from star formation and AGN, in combination with metal-line cooling, and the choice of IMF. The variation of  $SFR_{rec}/SFR$  and  $M_{*,rec}/M_*$  with galaxy mass in Figs. 6, 7, 9 and 10 is already suggestive of the important role played by these two feedback processes and we will

**Table 1.** Set of OWLS simulations that vary in terms of the feedback implementation (upper section) or the adopted IMF (lower section). From left to right, the columns show the model name, whether or not there is energy feedback associated with star formation (SF feedback), metal-line cooling and AGN feedback, the adopted IMF, the fraction of kinetic energy available from SN Type II that is used to drive galactic winds ( $f_{\text{th}}$ ), the initial wind velocity ( $v_w$ ) and the wind mass loading parameter ( $\eta$ ).

Name	SF feedback	Metal-line cooling	AGN feedback	IMF	$f_{\text{th}}$	$v_w$ [km/s]	$\eta$
Feedback variations							
<i>REF</i>	✓	✓	–	Chabrier	0.40	600	2.0
<i>NOZCOOL</i>	✓	–	–	Chabrier	0.40	600	2.0
<i>NOSN</i>	–	✓	–	Chabrier	0.40	600	2.0
<i>NOSN_NOZCOOL</i>	–	–	–	Chabrier	0.40	600	2.0
<i>AGN</i>	✓	✓	✓	Chabrier	0.40	600	2.0
IMF variations							
<i>IMFSALP</i>	✓	✓	–	Salpeter	0.66	600	2.0
<i>DBLIMFCONTSFML14</i>	✓	✓	–	Top-heavy <sup>a</sup>	0.40	600	14.6
<i>DBLIMFCONTSFV1618</i>	✓	✓	–	Top-heavy <sup>a</sup>	0.40	1618	2.0

<sup>a</sup> At high pressures ( $P/k > 2.0 \times 10^6 \text{ cm}^{-3} \text{ K}$ ) the IMF switches from Chabrier (2003) to a top-heavy power-law  $dN/dM \propto M^{-1}$ .

now show this explicitly. Furthermore, since the adopted IMF determines the fraction of the stellar mass that is released by a stellar population, we explore the effects of changing the IMF to bottom-heavy or top-heavy variants on recycling-fuelled star formation on galactic scales.

For our model comparison, we employ two sets of OWLS models: one in which the implementation of feedback is varied, by explicitly turning on or off a particular process, and one in which the adopted IMF is varied. These sets of variations are summarized in Table 1 and are described in more detail below. Although the EAGLE simulation suite also includes a set of physics variations featuring different feedback parameter choices, we revert to the OWLS simulation suite for the investigation in this section, as the OWLS physics variations are more extreme (i.e. a particular feedback or cooling process is switched on or off entirely). Moreover, unlike the EAGLE suite, the OWLS suite includes variations of the IMF<sup>9</sup>.

We start this section with a brief overview of the standard OWLS subgrid physics included in the simulations employed here, where we especially focus on the differences with respect to EAGLE (which was described in Section 3.1). In Sections 5.1 and 5.2, we compare for each set of OWLS model variations the value of  $SFR_{\text{rec}}/SFR$  as a function of halo mass ( $M_{200}$ ), where we do not treat central and satellite galaxies separately, but instead consider the total amount of star formation taking place within the FoF halo as a whole. Also, we do not apply an aperture when calculating  $SFR_{\text{rec}}/SFR$ . Although we do not explicitly show it, the results presented here also apply to  $M_{*,\text{rec}}/M_*$  as a function of halo mass, as well as for both ratios as functions of stellar mass.

The OWLS simulations were run with a modified version of the SPH code GADGET3, but in contrast with EAGLE it uses an entropy formulation of SPH (Springel & Hernquist 2002). For a detailed description of the differences in the hydrodynamical techniques and time stepping scheme between OWLS and EAGLE, we

refer the reader to S15. Here, we will instead focus on the differences in the subgrid physics. Each of the OWLS simulations used in this work was run in a periodic box of size  $L = 100 h^{-1} \text{ cMpc}$ .<sup>10</sup> The volume contains  $N = 512^3$  dark matter particles and an equal number of baryonic particles, having initial masses of  $m_{\text{dm}} = 4.1 \times 10^8 h^{-1} M_{\odot}$  and  $m_{\text{b}} = 8.7 \times 10^7 h^{-1} M_{\odot}$ , respectively. Unlike EAGLE, OWLS adopts cosmological parameters from WMAP 3-year data (Spergel et al. 2007), consistent with WMAP 7-year data (Komatsu et al. 2011):  $[\Omega_{\text{m}}, \Omega_{\text{b}}, \Omega_{\Lambda}, \sigma_8, n_s, h] = [0.238, 0.0418, 0.762, 0.74, 0.951, 0.73]$ . The gravitational softening length was switched from a fixed comoving scale to a fixed proper scale at  $z = 2.91$ .

Radiative cooling and heating and stellar evolution are implemented using the same prescriptions as in EAGLE. This means that the timed release of mass by an SSP, as we showed in Section 2, is valid for both EAGLE and OWLS. The implementation of star formation is still mostly consistent to that of EAGLE, although instead of a metallicity-dependent threshold, OWLS uses a fixed density threshold of  $n_{\text{H}}^* = 10^{-1} \text{ cm}^{-3}$ , above which gas particles are stochastically converted into star particles.

Important differences in the implementation of feedback include the model for the energy feedback associated with star formation, which in OWLS is implemented kinetically (following Dalla Vecchia & Schaye 2008) rather than thermally as in EAGLE. A fraction  $f_{\text{th}}$  of the energy available from star formation is injected locally, where it directly gives rise to galactic winds. Unlike the EAGLE model, in which  $f_{\text{th}}$  depends on local gas properties, OWLS keeps  $f_{\text{th}}$  fixed and equal to a fiducial value of 0.40. The launch of galactic winds by kinetic star formation feedback is realised by ‘kicking’ a fraction of the neighbouring gas particles of a newly formed star particle in random directions. In all but the IMF variation models, this is a kick of velocity  $v_w = 600 \text{ km s}^{-1}$ . The probability of receiving a kick is related to the wind mass loading parameter  $\eta$ , which is set to  $\eta = 2$  (except for the model within which this is explicitly varied). This means that the total mass of the gas particles being kicked is, on average, twice as high as the mass of the newly-formed star particle. The total kinetic energy injected into the winds is proportional to  $\eta v_w^2$ .

<sup>9</sup> Note that the OWLS subgrid models for stellar and AGN feedback are slightly different from the models used in EAGLE (as we describe below) and that the OWLS models do not reproduce the observed  $z \simeq 0$  GSMF as well as the EAGLE fiducial model. However, we can still use the suite of OWLS models to study the *relative* change in the SFR and stellar mass contributed by recycling upon changing the subgrid physics (at least qualitatively).

<sup>10</sup> Note that for OWLS, the box size and particle masses are given in units with  $h^{-1}$ .

Unlike EAGLE, in which prescriptions for the growth of BHs and the feedback from AGN are standard ingredients of the subgrid physics, BH growth and AGN feedback are only included in the OWLS model called *AGN*. In this simulation, the BH seeds, which have mass  $m_{\text{seed}} = 9 \times 10^4 M_{\odot}$  and are inserted in haloes more massive than  $m_{\text{halo,min}} = 4 \times 10^{10} M_{\odot}$ , can grow either through Eddington-limited Bondi Hoyle accretion or through mergers with other BHs. This implementation follows the model of Booth & Schaye (2009). The gas temperature increase in the model for thermal feedback from AGN (from Booth & Schaye 2009) is set to  $\Delta T = 10^8$  K, which is slightly lower than the value used in the fiducial EAGLE model ( $\Delta T = 10^{8.5}$  K).

In the following two sections, we list the model variations used in the respective section, and then present the comparison of  $SFR_{\text{rec}}/SFR$  as a function of halo mass among these models. The models will be referred to with the names given below and as listed in Table 1.

### 5.1 Effect of feedback processes and metal-line cooling

To investigate the effect of energy feedback from star formation and AGN on the contribution of recycled gas to the SFR and stellar mass of galaxies at  $z = 0$ , we consider a suite of OWLS models that vary in terms of their feedback implementation. We also explore the role of metal-line cooling, as this is closely related to the efficiency of the feedback. Note that these effects of feedback and metal-line cooling may not be independent.

- *REF* is the OWLS fiducial model, which serves as the reference in the model comparison. It includes radiative cooling and heating, star formation, stellar evolution and kinetic energy feedback from star formation. Note that it does *not* include prescriptions for BH growth and AGN feedback. All model variations listed below are varied with respect to this model.

- In *NOZCOOL* the cooling rates are calculated using primordial element abundances, i.e.  $X = 0.76$  and  $Y = 0.24$ .

- *NOSN* turns off all energy feedback mechanisms associated with star formation. However, the mass loss and metal production by massive stars, SN Type Ia and AGB stars are still present.

- *NOSN\_NOZCOOL* is a combination of the previous two models. It does not include galactic winds and the cooling rates are based on primordial element abundances.

- *AGN* includes models for the growth of BHs and feedback from AGN.

Fig. 11 shows the effects of star formation feedback, AGN feedback and metal-line cooling on  $SFR_{\text{rec}}/SFR$  as a function of halo mass,  $M_{200}$ . As before, the curves show median values in logarithmic bins of size 0.2 dex. For clarity, we only show the 10th to 90th percentile range (grey shaded region) for the OWLS reference model (black). The curves are shown as dotted lines where the haloes are less massive than 100 DM particles. Note that the mass scale corresponding to 100 DM is higher in OWLS than in the EAGLE simulation used in this work: the former is a factor of  $\sim 58$  higher due to the difference in resolution and the different units used for the box size (with  $h^{-1}$  for OWLS).

First comparing *NOSN* (green curve) to *REF* (black curve), we see that the feedback associated with star formation dramatically reduces the contribution of recycled gas to the SFR at all mass scales, in particular for  $M_{200} \lesssim 10^{12} M_{\odot}$ , where the regulation of star formation is largely governed by feedback from star formation. Here, the contribution drops from  $\sim 55\%$  (without star

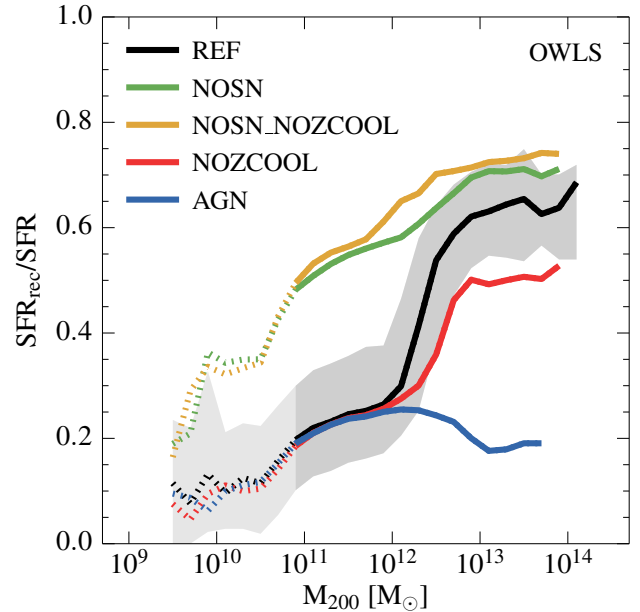


**Figure 11.** Comparison of a set of OWLS models to explore the effects of star formation feedback, AGN feedback and metal-line cooling on the contribution of recycled gas to the SFR at  $z = 0$ . The curves show the median (in logarithmic mass bins of size 0.2 dex containing at least 10 haloes) contribution of recycled gas to the SFR as a function of halo mass. The grey shaded region shows the 10th to 90th percentile region for the OWLS fiducial model (black curve). The solid curves become dotted when the halo mass corresponds to fewer than 100 DM particles. We find that the efficiency of the feedback associated with star formation (in low-mass galaxies) and the feedback of AGN (in high-mass galaxies) determines how much gas from stellar mass loss contributes to the SFR. A higher feedback efficiency results in a lower contribution from recycled gas.

formation feedback, *NOSN*) to  $\sim 25\%$  (with star formation feedback, *REF*). The large reduction can be explained if we consider the environments from which these star formation-driven winds are launched. The outflows originate in the dense ISM, which is the environment into which stellar mass loss is deposited. These stellar ejecta, which could be recycled into new generations of star formation, are prevented from forming stars if the winds eject the gas from the ISM in such a way that it does not return and become sufficiently dense again on short timescales. If, on the other hand, star formation feedback is inefficient, then this gas remains in the ISM and fuels star formation. The *REF* model shows an increasing  $SFR_{\text{rec}}/SFR$  with mass, which becomes increasingly similar to the *NOSN* model. This is consistent with SN feedback becoming less efficient as the depth of the potential well and the density and pressure in the ISM increase. Hence, the decreasing efficiency of the feedback leads to gas recycling being increasingly important for fuelling star formation in more massive systems.

A notable feature in the curve of the *REF* model is the sharp upturn of  $SFR_{\text{rec}}/SFR$  at a halo mass of  $M_{200} \sim 10^{12} M_{\odot}$ . Clearly, the feedback suddenly becomes very inefficient at this mass scale. As explained by Dalla Vecchia & Schaye (2012), this is due to strong artificial radiative losses in the ISM as the gas (which has a high pressure and density in these high-mass systems) gets shock-heated by the star formation-driven winds. Kinetic energy is thermalised to temperatures at which the cooling time is short relative to the sound crossing time, and is quickly radiated away.

As a consequence, the winds stall in the ISM before they can escape the galaxy, which drives up the value of  $SFR_{\text{rec}}/SFR$ . For a fixed initial velocity of the kinetically implemented winds, this effect causes a sharp transition at the mass scale for which artificial losses become significant. This results in unrealistic stellar mass fractions in haloes of  $M_{200} > 10^{12} M_{\odot}$  (Haas et al. 2013) and a failure of the model to reproduce the observed GSMF (Crain et al. 2009). Comparing *REF* to *NOZCOOL* (red), we see that the upturn becomes less pronounced if the cooling rates are reduced. Lower cooling rates, as a result of neglecting metal-line cooling (*NOZCOOL*), reduce the artificial thermal losses in the ISM and therefore enable the feedback to remain more efficient to higher mass scales. This results in lower values of  $SFR_{\text{rec}}/SFR$  in the most massive systems.

In addition to its impact upon the feedback efficiency, a change in the cooling rates also affects the accretion rate onto the galaxy, therefore impacting upon  $SFR_{\text{rec}}/SFR$  in a more direct fashion. However, from comparing *NOSN* (with metal-line cooling; green) and *NOSN\_NOZCOOL* (without metal-line cooling; yellow) we see that, in the absence of energy feedback associated with star formation, the effect of changing the cooling rates on  $SFR_{\text{rec}}/SFR$  is small, especially considering the expected amount of scatter in the two relations (from the grey shaded region). Hence, we conclude that a change in the cooling rates, as a result of turning metal-line cooling on or off, mainly affects the contribution of recycled gas to the SFR by changing the (partly numerical) efficiency of the star formation feedback implementation.

Finally, to investigate the effect of AGN feedback on  $SFR_{\text{rec}}/SFR$  as a function of halo mass, we compare the *AGN* model (blue curve), which includes AGN feedback, to the *REF* model. Since BHs live in the dense, central regions of galaxies, where a large fraction of the stellar ejecta are deposited, we again expect a low recycling-fuelled SFR if the AGN feedback is strong enough to eject gas from the ISM. The *AGN* model curve indeed shows that at masses  $M_{200} \gtrsim 10^{12} M_{\odot}$ , where feedback from AGN becomes important, the values of  $SFR_{\text{rec}}/SFR$  decrease towards higher masses. At a halo mass of  $M_{200} \sim 10^{13} M_{\odot}$ , recycled gas contributes only  $\sim 20\%$  to the SFR. This is in stark contrast to the *REF* model, for which the contribution reaches  $\sim 65\%$ , indicating the strong impact of AGN feedback on the  $SFR_{\text{rec}}/SFR$  in the regime where the feedback from star formation is inefficient and AGN are the main drivers of galactic winds. This highlights the importance of including AGN feedback in the subgrid model. Qualitatively, we conclude that for massive galaxies the increasing efficiency of AGN feedback towards higher masses leads to gas recycling being less important for fuelling present-day star formation.

## 5.2 Effect of changing the stellar initial mass function

To explore the effect of adopting an IMF different from the fiducial Chabrier (2003) IMF, we consider a second set of model variations. Comparing Figs. 1 and A1 already shows that the total mass and metal mass lost by an SSP is lower when the IMF of the population is more bottom-heavy (i.e. a Salpeter IMF). In addition, the cooling rate of the gas and the efficiency of the feedback from star formation and AGN are related to the metal mass and kinetic energy released by stellar populations, and are therefore also dependent on the choice of IMF. Hence, we also consider two model variations that use the surplus of stellar feedback energy from adopting a top-heavy IMF to increase either the velocity or the mass loading of galactic winds.

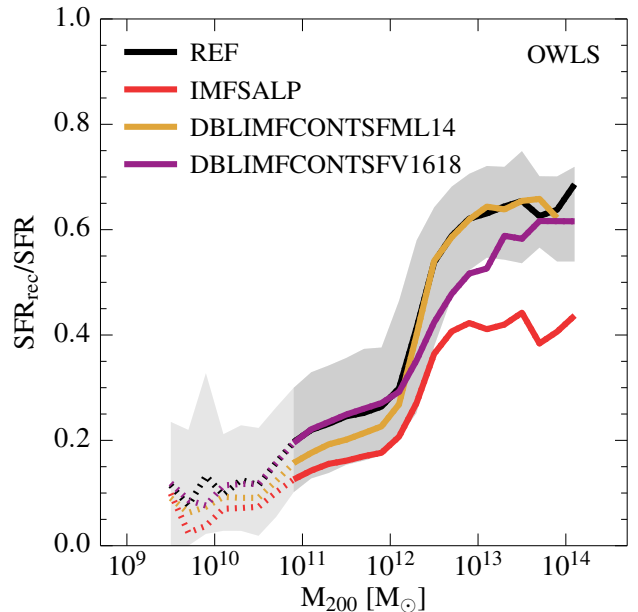


**Figure 12.** As Fig. 11, but showing a set of OWLS models with different IMFs. We find that adopting a more bottom-heavy (top-heavy) IMF reduces (enhances) the contribution from recycled gas to the SFR, but only if the fraction of feedback energy used to initiate star formation-driven galactic winds is kept fixed. If the extra stellar feedback energy from adopting a top-heavy IMF is used to either increase the mass loading or the wind velocity, then the recycled gas contributions decrease, showing that other IMF-related effects are more than compensated for by the increased efficiency of the star formation feedback.

- *IMFSALP* adopts a Salpeter (1955) IMF, spanning the same stellar mass range as the Chabrier (2003) IMF in our fiducial model. The corresponding change in the amplitude of the observed Kennicutt (1998) relation is taken into account. Note that the initial velocity and mass loading of star formation-driven winds are kept the same as in the reference model. This means that  $f_{\text{th}} = 0.40$  in the reference model is increased to  $f_{\text{th}} = 0.66$  in the *IMFSALP* model, while the total wind energy per unit stellar mass is kept fixed.

- *DBLIMFCONTSFML14* assumes an IMF that becomes top-heavy in high-pressure environments. For  $P/k > 2.0 \times 10^6 \text{ cm}^{-3} \text{ K}$  the IMF switches from a Chabrier power-law of  $dN/dM \propto M^{-2.3}$  to a more top-heavy power-law of  $dN/dM \propto M^{-1}$ . In these environments there is 7.3 times more stellar feedback energy available per unit stellar mass to drive galactic winds. In the *DBLIMFCONTSFML14* model the additional energy is used to increase the mass loading of the winds to  $\eta = 14.6$ , which is 7.3 times larger than in the reference model.

- As the previous model, *DBLIMFCONTSFV1618* switches to a top-heavy power-law IMF for stars forming in high-pressure regions. However, the extra energy from star formation is now used to increase the initial velocity of the winds:  $v_w$  is therefore  $\sqrt{7.3}$  times higher than in the reference model.

Fig. 12 shows the effect of adopting a different IMF than the fiducial Chabrier (2003) IMF. A comparison of *IMFSALP* (red curve) and *REF* (black curve) shows that adopting a more bottom-heavy IMF like Salpeter reduces the values of  $SFR_{\text{rec}}/SFR$  over the whole mass range. This was expected, because both the total mass and the metal mass released by stellar populations are lower

than for a Chabrier IMF (compare Figs. 1 and A1). In low-mass galaxies (in haloes with masses  $M_{200} \lesssim 10^{12} M_{\odot}$ ) the contribution of recycled gas to the SFR drops from  $\sim 25\%$  to  $\sim 15\%$ , while in high-mass galaxies it drops from  $\sim 65\%$  to  $\sim 40\%$ , upon changing the IMF from Chabrier to Salpeter. In these high-mass systems, we expect that the reduction is partly due to the reduction of the cooling rates and the slight increase of the efficiency of star formation feedback. This is the result of the reduced metal mass released by stellar populations, similar to disabling metal-line cooling in the *NOZCOOL* model (see Section 5.1). However, note that the amount of energy per unit stellar mass that is used to initiate the star formation-driven winds is kept fixed between the *REF* and *IMFSALP* models. Hence, differences in the  $SFR_{\text{rec}}/SFR$  between these two models are due to the differing fractions of the stellar mass available for recycling and the change in the cooling rates (which does affect the efficiency of the feedback).

Finally, we have two models, *DBLIMFCONTSFML14* and *DBLIMFCONTSFV1618*, that switch to a top-heavy IMF in high-pressure environments. This non-universal IMF leads to competing effects, since a top-heavy IMF yields more stellar mass loss, but also yields more stellar feedback energy to drive galactic winds, which is partly dissipated due the increased amount of metal mass loss. Comparing *REF* with *DBLIMFCONTSFML14* and *DBLIMFCONTSFV1618*, which differ in the way they make use of the surplus of feedback energy, enables us to determine which effect dominates. *DBLIMFCONTSFML14* uses the extra stellar feedback energy to increase the mass loading of the winds, while *DBLIMFCONTSFV1618* uses the energy to increase the initial wind velocity. We have investigated (but do not show here) the effects of increasing the mass loading or the initial wind velocity by comparing models that explicitly vary these parameters with respect to the fiducial model, without changing the IMF. We find that if the winds efficiently escape the galaxy (in low-mass systems,  $M_{200} \lesssim 10^{12} M_{\odot}$ ) the mass loading mainly determines the mass in gas that is ejected, whereas the initial velocity is of little importance. This is also what we see in Fig. 12, comparing *REF* to *DBLIMFCONTSFML14* (yellow curve) and *DBLIMFCONTSFV1618* (purple curve). Only the *DBLIMFCONTSFML14* model shows a small reduction of  $SFR_{\text{rec}}/SFR$  with respect to the *REF* model, indicating that the star formation feedback efficiency has slightly increased. On the other hand, in high-mass systems ( $M_{200} \gtrsim 10^{12} M_{\odot}$ ), where the artificial radiative losses are high and star formation-driven winds are not efficient in escaping the galaxy, we find that increasing the mass loading has little effect, as these losses remain too significant. Boosting instead the initial wind velocity, alleviates these losses and increases the efficiency of the wind, because the wind now thermalises at a higher temperature (Haas et al. 2013). This is also shown by the model curves in Fig. 12: at high mass, the values of  $SFR_{\text{rec}}/SFR$  for *DBLIMFCONTSFV1618* are somewhat reduced with respect to *REF*, illustrating the increased efficiency of the star formation feedback. Hence, we infer that the feedback efficiency is the dominating factor in determining  $SFR_{\text{rec}}/SFR$  as a function of halo mass. Despite the fact that, naively, we might have expected an increase of  $SFR_{\text{rec}}/SFR$  upon adopting a top-heavy IMF in high-pressure regions, as a result of the larger fraction of the stellar material available for recycling, the decrease of  $SFR_{\text{rec}}/SFR$  in the *DBLIMFCONTSFML14* and *DBLIMFCONTSFV1618* models compared to the *REF* model shows that this effect is more than compensated for by the increased efficiency of the star formation feedback.

From the OWLS model comparisons presented in this section we conclude that the efficiency of the feedback from star formation

and AGN is keys for regulating the fuelling of star formation with recycled gas. The choice of the IMF sets the total mass of gas that is potentially available for recycling, but the feedback efficiency determines how much gas recycled from stellar mass loss actually contributes to the SFR (and hence the stellar mass) of galaxies. This makes the contribution from recycled gas to the SFR and stellar mass sensitive to the mass of the galaxy.

## 6 SUMMARY AND DISCUSSION

We have investigated the significance of stellar ejecta as fuel for star formation using the *Ref-L100N1504* cosmological simulation from the EAGLE project. We studied the contribution of gas from evolved stellar populations to the SFR and stellar mass, as a cosmic average as a function of redshift and within individual galaxies as a function of metallicity and galaxy stellar mass at  $z = 0$ . We treated the galaxies identified as ‘centrals’ separately from those identified as ‘satellites’. Since the mass released by AGB stars, SN Type Ia and massive stars was explicitly followed in the simulation, we were able to assess the relative significance of these different mass loss channels for fuelling star formation. We also explored the radial dependence of gas recycling, by comparing the significance of recycling-fuelled star formation in the inner and outer parts of galaxies. Our results can be summarized as follows:

- The contribution of recycled gas to the present-day SFR and stellar mass of galaxies is strongly, positively correlated with, respectively, the metallicity of the ISM and stars. Therefore, many of our conclusions on the role of stellar ejecta in fuelling star formation as a function of galaxy mass and type carry over to the mass-metallicity relation. The relations between the contribution of stellar mass loss and metallicity do exhibit a slight dependence on galaxy stellar mass, as a result of the increasing contribution of mass loss from massive stars relative to that from intermediate-mass stars to the SFR and stellar mass for  $M_{*} \gtrsim 10^{10.5} M_{\odot}$  (Fig. 9, Section 4.3.3). We provide the best-fit relations (equations 8 and 9), including a term with the  $[O/Fe]$  abundance ratio, which enable one to estimate the importance of gas recycling in present-day galaxies from the observed metallicity and  $\alpha$ -enhancement (Fig. 4, Section 4.2).

- We apply the relations between the SFR contributed by recycling and ISM metallicity and between the stellar mass contributed by recycling and stellar metallicity from EAGLE to the observed mass-metallicity relations to estimate the recycled gas contributions as a function of galaxy stellar mass. Since we find these relations to be insensitive to the subgrid models for feedback, applying them to the observed mass-metallicity relations yields more accurate estimates for the contribution of recycling than the direct predictions of EAGLE, provided that the (systematic) uncertainty in the calibration of the observed mass-metallicity relation is smaller than the discrepancy between the mass-metallicity relation predicted by EAGLE and the observed relation. For central galaxies with a stellar mass similar to that of the Milky Way ( $M_{*} \sim 10^{10.5} M_{\odot}$ ), which corresponds to the mass scale of the peak in the galaxy formation efficiency, 35% of the present-day SFR and 20% of the present-day stellar mass is due to recycled stellar mass loss (Fig. 6, Section 4.3.1).

- Recycling of stellar mass loss becomes increasingly important for fuelling star formation towards lower redshift. At the present-day, the fiducial EAGLE model (i.e. as computed directly from the simulation) indicates that approximately 35% of the cosmic SFR

density and 19% of the cosmic stellar mass density is contributed by recycling (Figs. 2 and 3, Section 4.1).

- The fraction of the present-day SFR and stellar mass of central galaxies contributed by recycling shows a characteristic trend with the mass of the galaxy and its subhalo: for  $M_* \lesssim 10^{10.5} M_\odot$  ( $M_{\text{sub}} \lesssim 10^{12.2} M_\odot$ ) the contribution increases with mass, while for  $M_* \gtrsim 10^{10.5} M_\odot$  the contribution turns over and decreases with mass (in case of the SFR) or remains approximately constant (in case of the stellar mass). We infer that this trend is regulated by the efficiency of the feedback associated with star formation (at low mass scales) and AGN (at high mass scales). If feedback is efficient in driving galactic winds and thereby ejecting gas from the ISM, which is the environment into which stellar mass loss is deposited, then this will preferentially reduce the SFR and stellar mass contributed by recycled gas (Figs. 6 and 7, Section 4.3).

- The importance of gas recycling for fuelling ongoing star formation in satellite galaxies is broadly consistent with that for central galaxies over a wide range of masses, as recycling is mainly governed by the efficiency of feedback. However, the fiducial EA-GLE model indicates that in satellites with a Milky Way-like mass the fraction of the SFR contributed by recycled gas significantly exceeds the one in similarly massive centrals, and even reaches  $\gtrsim 90\%$  for satellites with the lowest gas fractions (Fig. 7, Section 4.3.2). We infer that this results from a depletion of the ISM gas reservoir of the satellite, either due to the cessation of fresh infall or the removal of gas from the disc, which makes them more reliant on stellar mass loss for fuelling ongoing star formation (Fig. 8, Section 4.3.2).

- As a cosmic average, the gas from AGB stars accounts for an increasing fraction of the recycled stellar mass loss towards lower redshift. At  $z \gtrsim 0.4$ , however, massive stars still provide the majority of the gas that fuels the cosmic SFR density through recycling. As a result, massive stars dominate the recycling-fuelled stellar mass density at all redshifts. The contribution from SN Type Ia is always small (Figs. 2 and 3, Section 4.1).

- Within individual galaxies, AGB stars and massive stars contribute approximately equally to the present-day SFR and stellar mass of centrals and satellites. The contribution from AGB stars to the SFR is slightly enhanced with respect to the massive star contribution at all but the highest mass scales, which results from the preferential ejection of massive star ejecta by star formation-driven winds and their early lock up in stellar remnants. At the highest mass scales ( $M_* \gtrsim 10^{10.5} M_\odot$ ), on the other hand, we find a relative enhancement in the contributions from massive stars, which we attribute to a downsizing effect, with more massive galaxies forming their stars earlier and more rapidly. Their stellar mass therefore preferentially consists of massive star ejecta, which are recycled on short timescales (Fig. 9, Section 4.3.3).

- Exploring the radial dependence of gas recycling within central and satellite galaxies, we find that recycling is more important for fuelling star formation (at the present-day and in the past) in the central parts of galaxies (within  $R_{50}$ ) than in the outskirts (outside  $R_{50}$ ), which is consistent with the observationally inferred inside-out growth of galaxies. We find that the difference between these two radial regimes is predominantly driven by the difference in the fractional contribution from AGB stars to the SFR (stellar mass), which is significantly higher than (roughly equal to) the one from massive stars inside  $R_{50}$  and roughly equal (lower) outside  $R_{50}$ . This radial trend directly reflects the negative stellar age gradient with increasing distance from the galactic centre (Fig. 10, Section 4.3.4).

Finally, we assessed the sensitivity of our results from the EA-GLE simulation to the physical processes in the subgrid model using a suite of simulations from the OWLS project (Schaye et al. 2010). The suite is comprised of a set of extreme variations of the feedback model, in which star formation feedback, AGN feedback and metal-line cooling are switched on or off entirely (Fig. 11, Section 5), as well as a set of variations of the adopted IMF (Fig. 12, Section 5). A systematic comparison of the results shows that while the total fraction of the stellar mass that is available for recycling is determined by the adopted IMF, the fraction of the stellar mass loss that is actually used to fuel star formation is controlled by the efficiency of the feedback associated with star formation and the feedback from AGN, each affecting the galaxy mass regime where the respective feedback process regulates the star formation.

Consistent with previous studies (e.g. Kennicutt et al. 1994; Leitner & Kravtsov 2011; Voit & Donahue 2011), our results emphasize the importance of modelling the recycling of stellar ejecta in simulations of galaxy formation, and the necessity of accounting for such gas in assessments of the ‘fuel budget’ of present-day galaxies. The fractional contribution of recycled ejecta to the SFR and stellar mass is not dominant, but it is also not negligible, and it extends the gas consumption timescale significantly beyond that implied by the ratio of the instantaneous gas mass and star formation rate of galaxies.

The relatively small contribution of recycling to the SFR and stellar mass of massive galaxies in our simulations is contrary to the naive expectation that the establishment of a hot circumgalactic medium quenches gas infall and renders the galaxy reliant on recycling for continued fuelling. Instead, the simulations indicate that the ongoing star formation in massive galaxies is sustained mostly by unprocessed gas. An interesting route for future studies will be to explore whether this gas originates in cooling flows, or is stripped from infalling satellite galaxies.

## ACKNOWLEDGEMENTS

This work used the DiRAC Data Centric system at Durham University, operated by the Institute for Computational Cosmology on behalf of the STFC DiRAC HPC Facility ([www.dirac.ac.uk](http://www.dirac.ac.uk)). This equipment was funded by BIS National E-infrastructure capital grant ST/K00042X/1, STFC capital grant ST/H008519/1, and STFC DiRAC Operations grant ST/K003267/1 and Durham University. DiRAC is part of the National E-Infrastructure. We also gratefully acknowledge PRACE for awarding us access to the resource Curie based in France at Trés Grand Centre de Calcul. This work was sponsored with financial support from the Netherlands Organization for Scientific Research (NWO), from the European Research Council under the European Union’s Seventh Framework Programme (FP7/2007-2013) / ERC Grant agreement 278594-GasAroundGalaxies, from the National Science Foundation under Grant No. NSF PHY11-25915, from the UK Science and Technology Facilities Council (grant numbers ST/F001166/1 and ST/I000976/1) and from the Interuniversity Attraction Poles Programme initiated by the Belgian Science Policy Office ([AP P7/08 CHARM]). RAC is a Royal Society University Research Fellow.

## REFERENCES

- Andrews B. H., Martini P., 2013, *ApJ*, **765**, 140  
 Asplund M., Grevesse N., Sauval A. J., Scott P., 2009, *ARA&A*, **47**, 481  
 Birnboim Y., Dekel A., 2003, *MNRAS*, **345**, 349

- Booth C. M., Schaye J., 2009, *MNRAS*, **398**, 53
- Brooks A. M., Governato F., Quinn T., Brook C. B., Wadsley J., 2009, *ApJ*, **694**, 396
- Cattaneo A., Dekel A., Faber S. M., Guiderdoni B., 2008, *MNRAS*, **389**, 567
- Chabrier G., 2003, *PASP*, **115**, 763
- Ciotti L., D’Ercole A., Pellegrini S., Renzini A., 1991, *ApJ*, **376**, 380
- Cowie L. L., Songaila A., Hu E. M., Cohen J. G., 1996, *AJ*, **112**, 839
- Crain R. A., et al., 2009, *MNRAS*, **399**, 1773
- Crain R. A., McCarthy I. G., Frenk C. S., Theuns T., Schaye J., 2010, *MNRAS*, **407**, 1403
- Crain R. A., McCarthy I. G., Schaye J., Theuns T., Frenk C. S., 2013, *MNRAS*, **432**, 3005
- Crain R. A., et al., 2015, *MNRAS*, **450**, 1937
- Creasey P., Theuns T., Bower R. G., 2015, *MNRAS*, **446**, 2125
- Dalla Vecchia C., Schaye J., 2008, *MNRAS*, **387**, 1431
- Dalla Vecchia C., Schaye J., 2012, *MNRAS*, **426**, 140
- Davis M., Efstathiou G., Frenk C. S., White S. D. M., 1985, *ApJ*, **292**, 371
- Dekel A., et al., 2009, *Nature*, **457**, 451
- Dolag K., Borgani S., Murante G., Springel V., 2009, *MNRAS*, **399**, 497
- Ferland G. J., Korista K. T., Verner D. A., Ferguson J. W., Kingdon J. B., Verner E. M., 1998, *PASP*, **110**, 761
- Fontanot F., De Lucia G., Monaco P., Somerville R. S., Santini P., 2009, *MNRAS*, **397**, 1776
- Furlong M., et al., 2015, *MNRAS*, **450**, 4486
- Gallazzi A., Charlot S., Brinchmann J., White S. D. M., Tremonti C. A., 2005, *MNRAS*, **362**, 41
- Gunn J. E., Gott III J. R., 1972, *ApJ*, **176**, 1
- Haardt F., Madau P., 2001, in Neumann D. M., Tran J. T. V., eds, *Clusters of Galaxies and the High Redshift Universe Observed in X-rays*. (arXiv:astro-ph/0106018)
- Haas M. R., Schaye J., Booth C. M., Dalla Vecchia C., Springel V., Theuns T., Wiersma R. P. C., 2013, *MNRAS*, **435**, 2931
- Hopkins P. F., 2013, *MNRAS*, **428**, 2840
- Kennicutt Jr. R. C., 1998, *ApJ*, **498**, 541
- Kennicutt Jr. R. C., Tamblyn P., Congdon C. E., 1994, *ApJ*, **435**, 22
- Kereš D., Katz N., Weinberg D. H., Davé R., 2005, *MNRAS*, **363**, 2
- Kereš D., Katz N., Fardal M., Davé R., Weinberg D. H., 2009, *MNRAS*, **395**, 160
- Kewley L. J., Ellison S. L., 2008, *ApJ*, **681**, 1183
- Komatsu E., et al., 2011, *ApJS*, **192**, 18
- Lagos C. d. P., et al., 2015, preprint, (arXiv:1503.04807)
- Larson R. B., Tinsley B. M., Caldwell C. N., 1980, *ApJ*, **237**, 692
- Leitner S. N., Kravtsov A. V., 2011, *ApJ*, **734**, 48
- Mac Low M.-M., Ferrara A., 1999, *ApJ*, **513**, 142
- Marigo P., 2001, *A&A*, **370**, 194
- Martin D. C., et al., 2007, *Nature*, **448**, 780
- Mathews W. G., 1990, *ApJ*, **354**, 468
- Mo H. J., Mao S., 2002, *MNRAS*, **333**, 768
- Moustakas J., Kennicutt Jr. R. C., Tremonti C. A., Dale D. A., Smith J.-D. T., Calzetti D., 2010, *ApJS*, **190**, 233
- Muñoz-Mateos J. C., Gil de Paz A., Boissier S., Zamorano J., Jarrett T., Gallego J., Madore B. F., 2007, *ApJ*, **658**, 1006
- Neistein E., van den Bosch F. C., Dekel A., 2006, *MNRAS*, **372**, 933
- Nelson D., Vogelsberger M., Genel S., Sijacki D., Kereš D., Springel V., Hernquist L., 2013, *MNRAS*, **429**, 3353
- Oppenheimer B. D., Davé R., 2008, *MNRAS*, **387**, 577
- Oppenheimer B. D., Davé R., Kereš D., Fardal M., Katz N., Kollmeier J. A., Weinberg D. H., 2010, *MNRAS*, **406**, 2325
- Parriott J. R., Bregman J. N., 2008, *ApJ*, **681**, 1215
- Pasquali A., Gallazzi A., van den Bosch F. C., 2012, *MNRAS*, **425**, 273
- Patel S. G., et al., 2013, *ApJ*, **766**, 15
- Peng Y.-j., Maiolino R., 2014, *MNRAS*, **438**, 262
- Planck Collaboration et al., 2014, *A&A*, **571**, A16
- Portinari L., Chiosi C., Bressan A., 1998, *A&A*, **334**, 505
- Putman M. E., et al., 2009, in *astro2010: The Astronomy and Astrophysics Decadal Survey*, p. 241 (arXiv:0902.4717)
- Rahmati A., Schaye J., Bower R. G., Crain R. A., Furlong M., Schaller M., Theuns T., 2015, preprint, (arXiv:1503.05553)
- Rees M. J., Ostriker J. P., 1977, *MNRAS*, **179**, 541
- Roberts M. S., 1963, *ARA&A*, **1**, 149
- Rosas-Guevara Y. M., et al., 2013, preprint, (arXiv:1312.0598)
- Salpeter E. E., 1955, *ApJ*, **121**, 161
- Sánchez S. F., et al., 2014, *A&A*, **563**, A49
- Sancisi R., Fraternali F., Oosterloo T., van der Hulst T., 2008, *A&A Rev.*, **15**, 189
- Sandage A., 1986, *A&A*, **161**, 89
- Sawala T., et al., 2015, *MNRAS*, **448**, 2941
- Schaller M., et al., 2015, *MNRAS*, **451**, 1247
- Schaye J., 2004, *ApJ*, **609**, 667
- Schaye J., Dalla Vecchia C., 2008, *MNRAS*, **383**, 1210
- Schaye J., et al., 2010, *MNRAS*, **402**, 1536
- Schaye J., et al., 2015, *MNRAS*, **446**, 521
- Silk J., 1977, *ApJ*, **211**, 638
- Spergel D. N., et al., 2007, *ApJS*, **170**, 377
- Springel V., 2005, *MNRAS*, **364**, 1105
- Springel V., Hernquist L., 2002, *MNRAS*, **333**, 649
- Springel V., White S. D. M., Tormen G., Kauffmann G., 2001, *MNRAS*, **328**, 726
- Springel V., Di Matteo T., Hernquist L., 2005, *MNRAS*, **361**, 776
- Thielemann F.-K., et al., 2003, in Hillebrandt W., Leibundgut B., eds, *From Twilight to Highlight: The Physics of Supernovae*. p. 331, doi:10.1007/10828549\_46
- Thomas D., Maraston C., Schawinski K., Sarzi M., Silk J., 2010, *MNRAS*, **404**, 1775
- Tremonti C. A., et al., 2004, *ApJ*, **613**, 898
- Voit G. M., Donahue M., 2011, *ApJ*, **738**, L24
- Wiersma R. P. C., Schaye J., Smith B. D., 2009a, *MNRAS*, **393**, 99
- Wiersma R. P. C., Schaye J., Theuns T., Dalla Vecchia C., Tornatore L., 2009b, *MNRAS*, **399**, 574
- Woolsey S. E., Weaver T. A., 1995, *ApJS*, **101**, 181
- Zahid H. J., Dima G. I., Kudritzki R.-P., Kewley L. J., Geller M. J., Hwang H. S., Silverman J. D., Kashino D., 2014, *ApJ*, **791**, 130
- Zaritsky D., Kennicutt Jr. R. C., Huchra J. P., 1994, *ApJ*, **420**, 87
- van de Voort F., Schaye J., 2012, *MNRAS*, **423**, 2991
- van de Voort F., Schaye J., Booth C. M., Haas M. R., Dalla Vecchia C., 2011, *MNRAS*, **414**, 2458

## APPENDIX A: MASS RELEASED BY AN SSP WITH A SALPETER IMF

Fig. A1 shows the total (left) and metal (right) mass released by an SSP with a Salpeter (1955) IMF (solid lines) and by an SSP with a Chabrier (2003) IMF (dotted lines) in the range  $0.1 - 100 M_{\odot}$  as a function of age for solar metallicity. The colours in both panels have the same meaning as in Fig. 1. The (metal) mass loss is lower for a Salpeter IMF than for a Chabrier IMF by a factor of  $\sim 1.5$  over the whole range of SSP ages plotted. The relative contributions from massive stars and AGB stars are somewhat lower and higher, respectively. The metal mass loss from SN Type Ia is higher for a Salpeter IMF, accounting for  $\sim 8\%$  of the total metal mass released. In general, adopting a Salpeter IMF instead of a Chabrier IMF increases the relative contributions from intermediate-mass stars to the (metal) mass loss, as expected for a more bottom-heavy IMF.

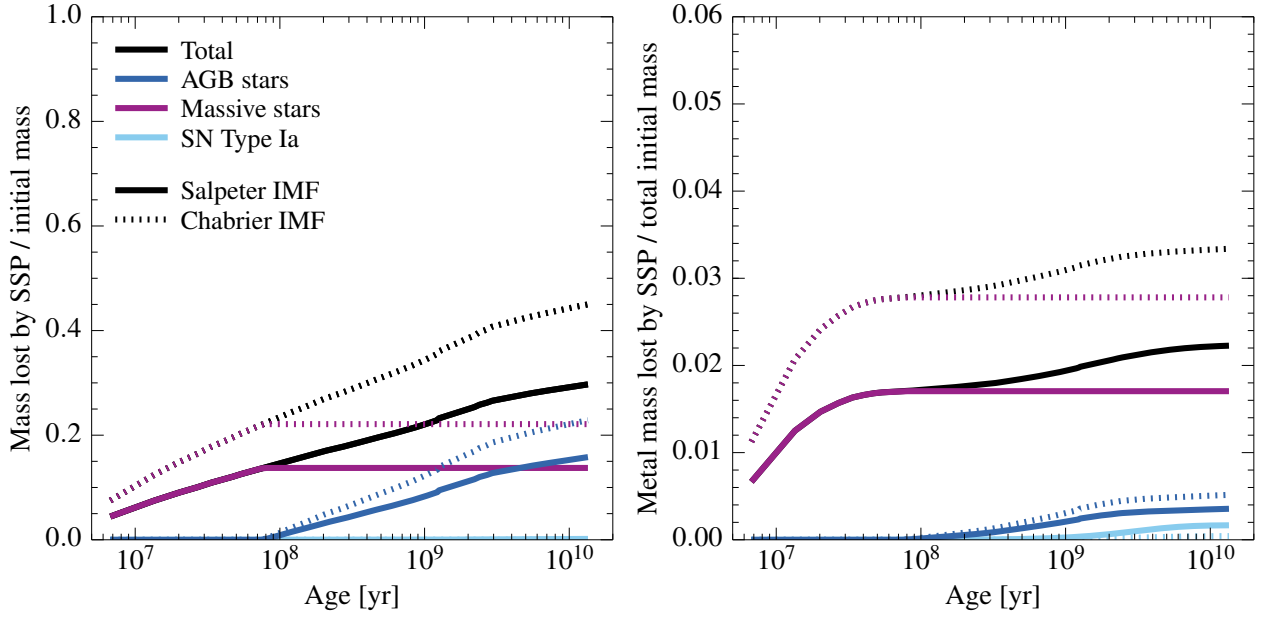


**Figure A1.** The cumulative fraction of the initial mass (total: left panel; in the form of metals: right panel) that is released by an SSP as a function of its age, adopting a [Salpeter \(1955\)](#) IMF (solid lines) or a [Chabrier \(2003\)](#) IMF (dotted lines). The curves show the contributions from AGB stars (blue), massive stars (purple) and SN Type Ia (cyan), as well as the total (metal) mass ejected by the SSP (black) for solar stellar metallicity. The total (metal) mass loss is lower for a Salpeter IMF than for a Chabrier IMF by a factor of  $\sim 1.5$ . Adopting a Salpeter IMF increases the relative contributions from AGB stars and SN Type Ia, which have intermediate-mass progenitor stars.

## APPENDIX B: NUMERICAL CONVERGENCE

### B1 Relation between recycled gas contributions and stellar mass

We test for numerical convergence with respect to resolution of the  $SFR_{\text{rec}}/SFR - M_*$  and  $M_{*,\text{rec}}/M_* - M_*$  relations using a set of three EAGLE simulations that were run in volumes of size  $L = 25$  cMpc. We consider both ‘weak’ and ‘strong’ convergence (following the nomenclature introduced by S15) by comparing simulations with recalibrated and non-recalibrated subgrid physics, respectively. We use:

- One simulation with  $N = 376^3$  and with the same subgrid model parameters as our fiducial  $L = 100$  cMpc,  $N = 1504^3$  simulation that was used throughout this work. This simulation (denoted *Ref-L025N376*) has the same resolution as the fiducial simulation.
- One simulation with  $N = 752^3$  and the same subgrid model parameters as the fiducial simulation, but with 8 times higher mass resolution (*Ref-L025N752*).
- One simulation with  $N = 752^3$  and with a *recalibrated* set of subgrid model parameters for star formation feedback, AGN feedback and the accretion onto BHs, in order to improve the match with the observed  $z \simeq 0$  GSMF at this 8 times higher mass resolution (*Recal-L025N752*). In short, the recalibration corresponds to a change in the density dependence of the stellar feedback efficiency parameter  $f_{\text{th}}$ , such that the feedback efficiency is increased in higher-density gas while keeping the average  $f_{\text{th}}$  roughly equal to 1. This is done in order to compensate for the increase in cooling losses, which arise as a result of the locally higher gas densities that are resolved in the higher-resolution model.

A comparison of these three EAGLE simulations is shown in Fig. B1, where we plot  $SFR_{\text{rec}}/SFR$  (top) and  $M_{*,\text{rec}}/M_*$  (bottom) as a function of stellar mass. We show these relations for both central galaxies (left) and satellite galaxies (right). Since our conclusions about resolution convergence are broadly consistent between centrals and satellites (although with somewhat poorer sampling for the latter), we will focus the discussion below on central galaxies.

Comparing the fiducial resolution simulation (*Ref-L025N0376*; red) to the two higher-resolution simulations, with (*Recal-L025N0752*; purple) and without (*Ref-L025N0752*; blue) recalibrated subgrid feedback parameters, we infer that for central galaxies with  $M_* \lesssim 10^{9.8} M_\odot$ ,  $SFR_{\text{rec}}/SFR$  and  $M_{*,\text{rec}}/M_*$  as a function of stellar mass are not numerically converged at the fiducial resolution. The ‘strong’ convergence is somewhat better than the ‘weak’ convergence. At  $M_* \sim 10^9 M_\odot$ ,  $SFR_{\text{rec}}/SFR$  and  $M_{*,\text{rec}}/M_*$  in *Ref-L025N0376* are almost a factor of 2 (0.3 dex on a logarithmic scale) higher than in *Recal-L025N0752*. This is not surprising considering the level of agreement between *Ref-L100N1504* and *Recal-L025N0752* for the mass-metallicity relations, where the latter is in better agreement with the observations (see fig 13. of S15).

At masses  $M_* \gtrsim 10^{9.8} M_\odot$ , the relation between  $M_{*,\text{rec}}/M_*$  and stellar mass is fully converged (both ‘weakly’ and ‘strongly’), while  $SFR_{\text{rec}}/SFR$  as a function of stellar mass shows substantial overlap between *Ref-L025N0376*, *Ref-L025N0752* and *Recal-L025N0752*. Due to the small box size, however,  $SFR_{\text{rec}}/SFR$  is not well-sampled around  $M_* \sim 10^{10.5} M_\odot$ , the mass scale at which  $SFR_{\text{rec}}/SFR$  reaches a maximum in our fiducial  $L = 100$  cMpc model (see Fig. 6).



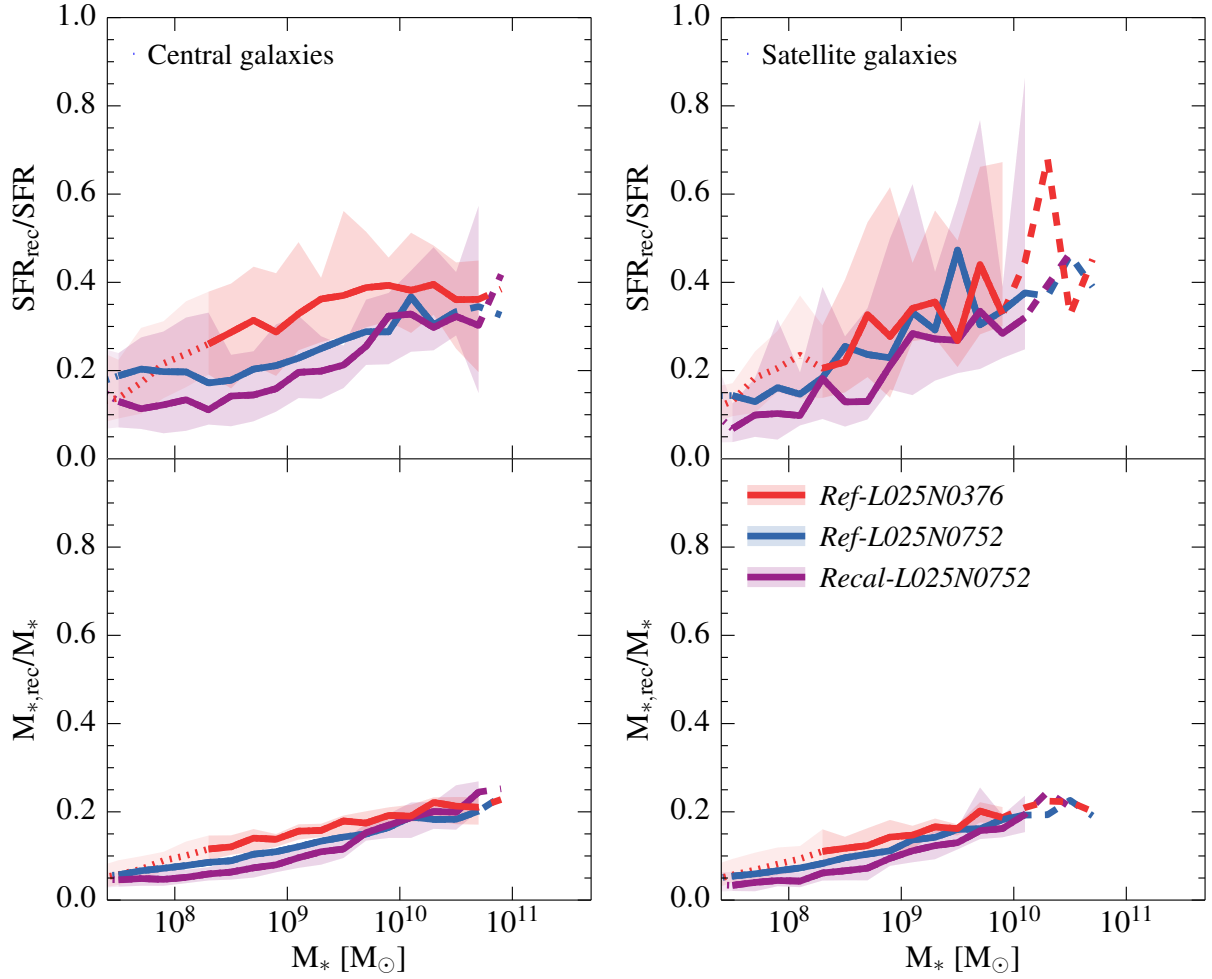


**Figure B1.** Test for numerical convergence of the  $SFR_{\text{rec}}/SFR - M_*$  (top) and  $M_{*,\text{rec}}/M_* - M_*$  (bottom) relations (presented in Figs. 6 and 7) for central (left) and satellite (right) galaxies at  $z = 0$ , comparing an EAGLE simulation with the fiducial resolution (*Ref-L025N0376*; red) to two EAGLE simulations with 8 times higher mass resolution, with (*Recal-L025N0752*; purple) and without (*Ref-L025N0752*; blue) recalibrated subgrid feedback parameters. All three simulations were run in volumes of size  $L = 25$  cMpc. The curves and shaded regions have the same meaning as in Fig. 6, but for clarity we only show the 10th to 90th percentile range for the *Ref-L025N0376* and *Recal-L025N0752* simulations. For galaxies with  $M_* \gtrsim 10^{9.8} M_\odot$ ,  $SFR_{\text{rec}}/SFR$  and  $M_{*,\text{rec}}/M_*$  as a function of stellar mass are reasonably well converged. For galaxies with  $M_* \lesssim 10^{9.8} M_\odot$ , the fiducial EAGLE simulation likely overpredicts the SFR and stellar mass contributed by recycling, by at most a factor of  $\sim 2$  ( $\sim 0.3$  dex) at  $M_* \sim 10^9 M_\odot$ .

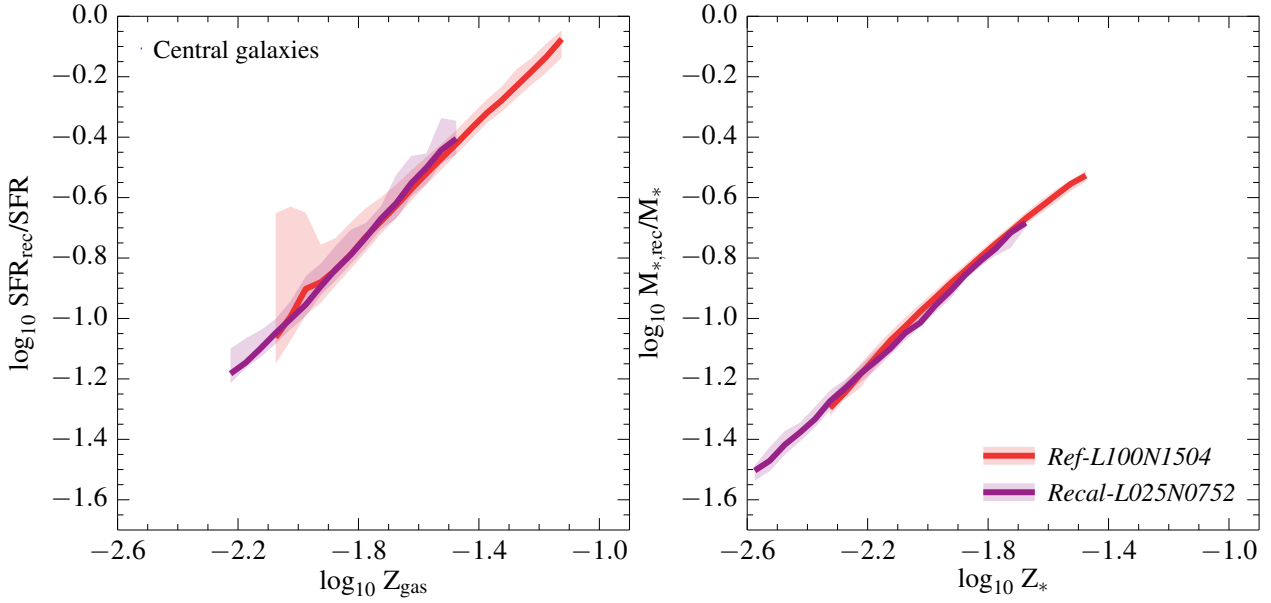
## B2 Relation between recycled gas contributions and metallicity

Fig. B2 shows the numerical convergence test of the  $SFR_{\text{rec}}/SFR - Z_{\text{gas}}$  (left) and  $M_{*,\text{rec}}/M_* - Z_*$  (bottom) relations for central galaxies, comparing the fiducial EAGLE model (*Ref-L100N1504*; red) and the high-resolution, recalibrated model (*Recal-L025N0752*; purple). While *Recal-L025N0752* spans a metallicity range that is shifted towards somewhat lower values with respect to *Ref-L100N1504*, due to its smaller box size and 8 times higher mass resolution (we select stellar masses corresponding to at least 100 gas particles at each resolution), the  $SFR_{\text{rec}}/SFR - Z_{\text{gas}}$  and  $M_{*,\text{rec}}/M_* - Z_*$  are converged with resolution over the whole metallicity range probed here. Where *Recal-L025N0752* and *Ref-L100N1504* overlap, their medians agree to better than 0.05 dex in  $SFR_{\text{rec}}/SFR$  and to better than 0.04 dex in  $M_{*,\text{rec}}/M_*$ .

## APPENDIX C: EFFECT OF USING A 3D APERTURE

Fig. C1 shows the effect of using a 30 pkpc 3D aperture on the contribution of recycled gas to the SFR (top) and stellar mass (bottom) in central galaxies at  $z = 0$  as a function of their subhalo mass (left) and stellar mass (right). We compare results from the EAGLE fiducial model, *Ref-L100N1504*, with (red) an without (purple) the aperture. Recall that the aperture only applies to galaxy properties, hence the subhalo mass is not affected.

While the majority of the star formation takes places within the central 30 pkpc, causing the effect of the aperture on the total SFR to be small, there is still an enhancement in  $SFR_{\text{rec}}/SFR$  (upper panels) inside the aperture compared to its value over the whole galaxy. This enhancement is consistent with recycling-fuelled star formation being more important in the central parts of galaxies (see Fig. 10). The effect is significant for  $M_* \gtrsim 10^{11} M_\odot$  ( $M_{\text{sub}} \gtrsim 10^{12.5} M_\odot$ ) and increases with mass up to a difference of a factor of  $\sim 1.5$  ( $\sim 0.18$  dex) in the left panel, whereas in the right panel



**Figure B2.** Test for numerical convergence of the  $SFR_{\text{rec}}/SFR$ - $Z_{\text{gas}}$  (left) and  $M_{*,\text{rec}}/M_*$ - $Z_*$  (right) relations (presented in Fig. 4) for central galaxies at  $z = 0$ , comparing the fiducial EAGLE model (*Ref-L100N1504*; red) and the high-resolution, recalibrated model (*Recal-L025N0752*; purple). We only consider galaxies with stellar masses corresponding to at least 100 gas particles, at the respective resolution. In the left panel we only consider subhaloes with a non-zero SFR. The curves show the median value in each logarithmic metallicity bin of size 0.05 dex, if it contains at least 10 galaxies. The shaded regions mark the 10th to 90th percentile ranges. The  $SFR_{\text{rec}}/SFR$ - $Z_{\text{gas}}$  and  $M_{*,\text{rec}}/M_*$ - $Z_*$  relations are converged at the fiducial resolution over the whole metallicity range.

the effect is smaller (up to a factor of  $\sim 1.2$ , or  $\sim 0.08$  dex) due to the simultaneous decrease in the stellar mass if an aperture is applied.

Similarly, in the lower panels,  $M_{*,\text{rec}}/M_*$  is enhanced if an aperture is applied. In this case, the effect of using an aperture is that the decrease of  $M_{*,\text{rec}}/M_*$  with mass for  $M_* \gtrsim 10^{10.5} M_{\odot}$  ( $M_{\text{sub}} \gtrsim 10^{12.2} M_{\odot}$ ) becomes a flattening at a roughly constant value ( $\sim 22\%$  instead of  $17\%$  at  $M_* \sim 10^{11.5} M_{\odot}$ ).

This paper has been typeset from a  $\text{\TeX}/\text{\LaTeX}$  file prepared by the author.

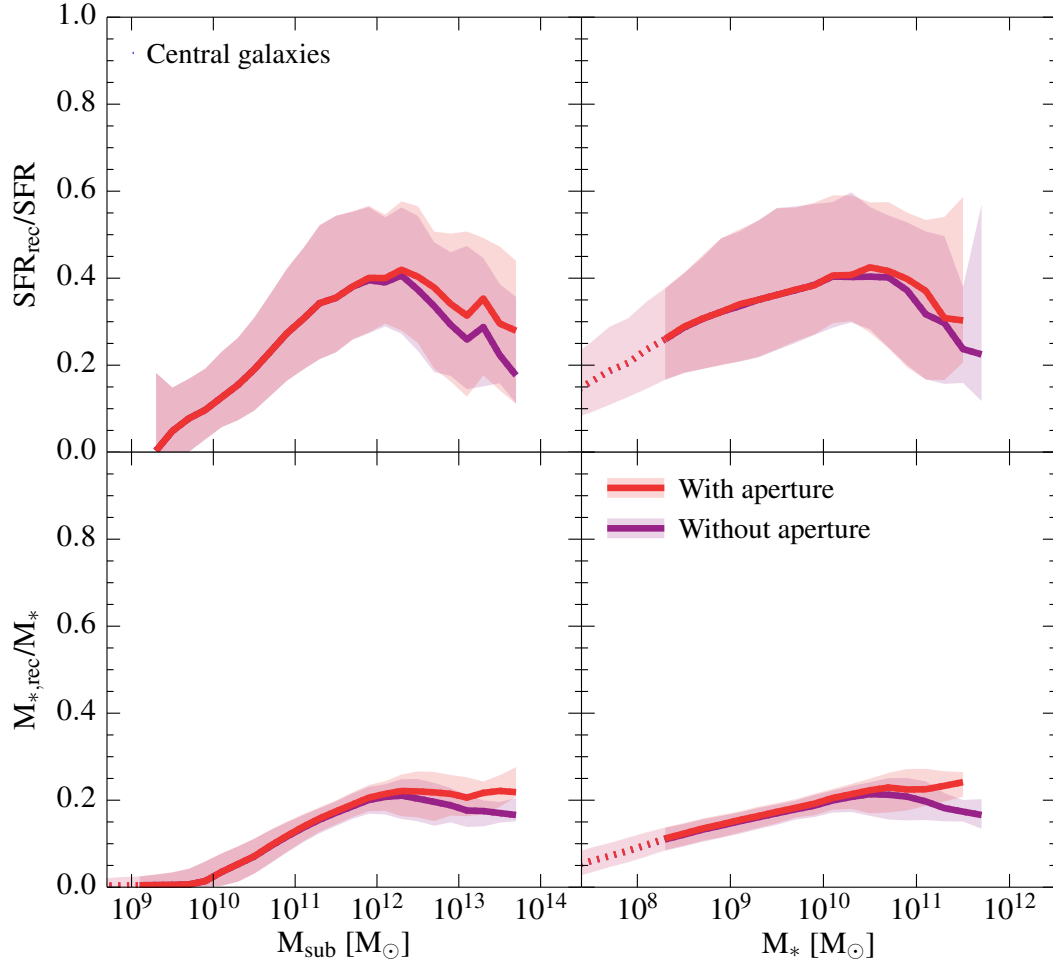


**Figure C1.** The effect of using a 30 pkpc 3D aperture, comparing results from the EAGLE fiducial model, *Ref-L100N1504*, with (red) and without (purple) applying the aperture in calculating galaxy properties. The curves show the fraction of the SFR (top) and stellar mass (bottom) contributed by recycling for central galaxies at  $z = 0$  as a function of their subhalo mass (left) and stellar mass (right). The curves and shaded regions have the same meaning as in Fig. 6. The effect of using an aperture is a change in the slope of the two recycled gas fractions at  $M_* \gtrsim 10^{11} M_{\odot}$  ( $M_{\text{sub}} \gtrsim 10^{12.5} M_{\odot}$ ), which becomes somewhat shallower. For the fraction of the stellar mass contributed by recycling this results in a roughly flat trend instead of a decrease with subhalo and stellar mass, hence mitigating the effect of increasing AGN feedback efficiency.